energies

MDPI

Article

An Asymptotic Energy Equation for Modelling Thermo Fluid Dynamics in the Optical Fibre Drawing Process

Giovanni Luzi [1,*], Seunghyeon Lee [2], Bernhard Gatternig [3] and Antonio Delgado [1]

[1] LSTME Busan, Busan 46742, Korea
[2] Department of Energy and Machine Engineering, Gyeongsang National University, Tongyeong 53064, Korea
[3] Department of Environmental Engineering, Hochschule Weihenstephan-Triesdorf, 91746 Weidenbach, Germany
* Correspondence: giovanni.luzi@lstme.org

Abstract: Microstructured optical fibres (MOFs) are fibres that contain an array of air holes that runs through the whole fibre length. The hole pattern of these fibres can be customized to manufacture optical devices for different applications ranging from high-power energy transmission equipment to telecommunications and optical sensors. During the drawing process, the size of the preform is greatly scaled down and the original hole pattern result might be modified, potentially leading to unwanted optical effects. Because only a few parameters can be controlled during the fabrication process, mathematical models that can accurately describe the fibre drawing process are highly desirable, being powerful predictive tools that are significantly cheaper than costly experiments. In this manuscript, we derive a new asymptotic energy equation for the drawing process of a single annular capillary and couple it with existing asymptotic mass, momentum, and evolution equations. The whole asymptotic model only exploits the small aspect ratio of a capillary and relies on neither a fitting procedure nor on any empirical adjustable parameters. The numerical results of the simplified model are in good accordance with experimental data available in the literature both without inner pressurization and when internal pressure is applied. Although valid only for annular capillaries, the present model can provide important insights towards understanding the MOF manufacturing process and improving less detailed approaches for more complicated geometries.

Keywords: asymptotic analysis; optical fibre drawing; creeping flow; energy equation; MOFs

check for updates

Citation: Luzi, G.; Lee, S.; Gatternig, B.; Delgado, A. An Asymptotic Energy Equation for Modelling Thermo Fluid Dynamics in the Optical Fibre Drawing Process. *Energies* **2022**, *15*, 7922. https://doi.org/10.3390/en15217922

Academic Editors: Artur Bartosik and Dariusz Asendrych

Received: 19 October 2022
Accepted: 20 October 2022
Published: 25 October 2022

Publisher's Note: MDPI stays neutral with regard to jurisdictional claims in published maps and institutional affiliations.

Copyright: © 2022 by the authors. Licensee MDPI, Basel, Switzerland. This article is an open access article distributed under the terms and conditions of the Creative Commons Attribution (CC BY) license (https://creativecommons.org/licenses/by/4.0/).

1. Introduction

Microstructured optical fibres (MOFs) or Photonic Crystal Fibres (PCFs) are a new kind of optical fibres, appearing for the first time approximately thirty years ago [1]. This new type of fibres possesses an array of air holes arranged in a specific pattern that spans the whole fibre length. Light guidance within PCFs relies either on the index guiding or on the photonic bandgap (PBG) mechanism. If the central air capillary is removed from the structure, the electromagnetic waves are guided by a modified total internal reflection mechanism. Conversely, if the central air capillary is replaced with another one of a different size, the PBG mechanism is realized [2]. The network of air holes can be suitably designed to allow for the guidance of selected modes. This can be achieved with specific ratios between the diameter of an air capillary and the crystal lattice constant. Many advantages of this new type of fibres are represented by the high degree of flexibility and many possibilities they offer. PCFs find a large number of applications, ranging from high-power and energy transmission [3], fibre lasers [4] and amplifiers [5], Kerr-related nonlinear effects [6], Brillouin scattering [7], telecommunications [1], and optical sensors [8–12], among others.

The manufacturing process of glass optical fibres presupposes two steps. First, a fibre-preform is manufactured, and afterward it is drawn inside a high-tech furnace incorporated

in a tower set-up. Fibre preforms are built by stacking silica capillary tubes and solid rods. This allows for quick, low-cost, and flexible manufacturing of preforms. After stacking, capillaries and rods are seized together by thin wires and eventually fused in an intermediate drawing process in which the structures do not achieve the required final dimensions, but are instead drawn into an intermediate preform-cane. A large number of preform-canes are usually manufactured, as they can be utilized for the development and optimization of different PCFs structures. During the drawing process, holes might experience distortion and positions and sizes might be altered. This occurs because the drawing process takes place at elevated temperatures and surface tension may lead to the collapse of the internal holes that form the air lattice. Therefore, internal pressurization is commonly applied to prevent hole collapse. An alternative to glass MOFs is represented by microstructured polymer optical fibres (MPOFs) [13]. They have several advantages compared to glass MOFs. For instance, the processing temperature of polymers is much lower than that of the glass, and the polymerization processes are easier to control. This entails the utilization of different techniques to produce polymer preforms of arbitrary cross-section arrangements, such as extrusion, polymer coating, polymerization in a mold, and injection molding [14]. Another advantage of MPOFs is that they can be drawn over a wide temperature range without significant changes in the fibre structure, unlike glass MOFs, for which temperature variations of just a few percentage points can induce significant variations in the fibre microstructure. In addition, the high temperatures involved in the fabrication of glass MOFs hinder the possibility of modifying the optical properties using dopants, as phase separation may occur [14]. Conversely, MPOFs can be easily doped with atomic species, molecular components, dispersed molecules, and phases. Moreover, the lower temperatures involved in the fabrication process of MPOFs reduce the chances of hole collapse and allow low cost production in large volumes, as both the material and the production process are cheaper [15]. Independently of the material used to fabricate MOFs, accurate control of fibre structures concerning hole dimensions and position is essential for the manufacturing of PCFs with specific properties. The inclusion or elimination of interstitial holes can have dramatic consequences on the final fibre properties. The key element in the drawing process of PCFs is the ability to maintain the highly regular structure down to the final dimensions.

Mathematical models and numerical simulations that can describe the fibre drawing process are highly desirable, as they allow for understanding and quantifying the transport phenomena and main physical quantities involved in the process. Furthermore, they represent more valid predictive and process control tools compared to expensive experiments. To this end, many theoretical and numerical studies have been carried out over the past fifty years. Early studies mainly focused on one-dimensional drawing models of solid fibres. Peak and Runk [16] derived a simplified model consisting of axial momentum and energy equations with a simplified radiation model to predict the neck shape and the temperature distribution of a silica rod during the drawing process. Myers [17] extended Glicksman's model [18] by introducing a radiative heat transfer model that considers the slope of preform surfaces, the spectral variation of the glass properties, and the dependencies of the emissivity on the fibre diameter. Fitt et al. [19] utilized asymptotic techniques to derive a model that describes the drawing process of a capillary and examined it on selected asymptotic limits to isolate and quantify the effects of main physical parameters on the drawing process. Luzi et al. [20] numerically solved the asymptotic model of Fitt et al. [19] by assuming Gaussian distributions of the temperature profile inside the furnace. The numerical results are in good accordance with the experimental ones, both for the case of an unpressurized capillary and for the case when the inner pressurization is applied. In a series of contributions, Voyce et al. [21–23] extended the previous work by Fitt et al. [19] by including the effect of preform rotation in their model. Rotation is particularly useful to control Polarization Mode Dispersion (PMD) and fibre birefringence effects, as well as to tune the capillary size. More recently, Taroni et al. [24] utilized asymptotic analysis to derive simplified momentum and energy equations to describe the drawing process of a

solid fibre while considering the heat transport within the fibre via conduction, convection, and radiative heating.

Numerical investigations of the drawing process of fibres with more complicated cross-sectional structures have been initially carried out using finite element-based commercial software. In a two-series contribution, Xue et al. [25] first performed a scaling analysis of the governing equations to determine the importance of the main parameters involved in the drawing process. Afterwards, they simulated the transient drawing process of MOFs containing five holes, showing that the shape of the holes changes dramatically in the vicinity of the neck-down region. In the subsequent manuscript, Xue et al. [26] investigated the steady-state process, focusing on the effects of surface tension, viscosity, and stress redistribution within the fibre. Non-isothermal simulations revealed that the slope of the neck-down region is highly sensitive to the viscosity profile, and therefore to temperature gradients. In a different work, Xue et al. [27] scrutinized the mechanism of hole deformation for silica and polymer fibres. To this end, they simulated the drawing process of a five-hole and polarization-maintaining structure, focusing on hole deformation and hole expansion in terms of the capillary number, draw, and aspect ratio. Luzi et al. [28] modeled the drawing process of six-hole MOFs, obtaining very good agreement between numerical simulations and experiments as long as the applied inner pressurization was not too high. Even in that case, the shape of the deformed holes was in qualitatively good agreement with the experimental one. Nevertheless, solving the full three-dimensional problem proves numerically expensive, and significant computational resources are often needed.

To cope with this issue, Stokes et al. [29] presented a general mathematical framework to model the drawing process of optical fibres of general cross-sectional shape, with the only requirement that the fibre must be slender. Chen et al. [30] extended the work of Stokes et al. [29] by including channel pressurization. Buchak et al. [31] developed the generalized Elliptical Pore Model (EPM), a very efficient method for cases in which the fibre cross-section contains elliptical holes. The evolution of an inner hole is determined by the solution of a set of ordinary integrodifferential equations that determine the centroid position, orientation, area, and eccentricity along the drawing direction. In a different contribution, Buchak and Crowdy [32] employed spectral methods with conformal mapping to obtain a very accurate reconstruction of the cross-sectional shape. Chen et al. [33] utilized the numerical approach of Buchak and Crowdy [32] to model the drawing process of a six-hole MOF and compared the results with the experiments and the Finite Element Method (FEM)-based simulations by Luzi et al. [28]. The approach used by [33] allows for accurate computation of the hole-interface curvature and is in better agreement with experimental results compared with the FEM simulations, and is significantly more computationally efficient. However, in these contributions, the heat transfer between the furnace and the fibre is not modelled, and the drawing is assumed to be isothermal with an assumed fibre temperature profile. In a recent manuscript, Stokes et al. [34] derived an asymptotic energy equation for the full three-dimensional problem utilizing only asymptotic analysis based on the small fibre aspect ratio and coupled it with the generalized EPM of Buchak et al. [31]. Jasion et al. [35] proposed the MicroStructure Element Method (MSEM) for modeling the drawing process of MOFs with a high filling fraction and thin glass membranes, such as Hollow Core Photonic Crystal fibres (HC-PCFs). They used the model of Fitt et al. [19] to describe the evolution of the external jacket that surrounds the microstructured array of air-holes with a network of fluid struts linked through nodes where surface tension, viscous, and pressure force act. However, the energy equations utilized in these two contributions consider neither the heat transfer across the fibre cross-section nor the viscous diffusion.

Detailed numerical investigations concerning the conjugate heat transfer between the fibre and the furnace have been carried out by different researchers. Lee and Jaluria [36] simulated the conjugate heat transfer between the furnace and solid fibre assuming an axis-symmetric geometry and a given distribution of the fibre shape. Chodhury and Jaluria [37] investigated the effects of the fibre draw speed, inert gas velocity, furnace dimensions, and gas properties on the temperature distribution within a solid glass fibre and an oven. Yin

and Jaluria [38] utilized the zonal method and the optically thick approximation to compute the radiative heat exchange between the furnace and solid glass fibre. Their numerical investigations reveal that the zonal method can predict the radiative flux with reasonable accuracy independently of the temperature distribution within the fibre, although the optically thick approximation can only predict a correct temperature distribution when the radial temperature distribution is small. In a subsequent contribution, Yin and Jaluria [39] utilized the zonal method and the optically thick approximation with a force balance to generate neck-down profiles of a solid fibre. On the one hand, the difference between the profiles generated using the zonal method and the optically thick approximation is not very large. On the other hand, other parameters have a significant influence on the thermal neck-down profiles, that is, the fibre drawing speed and the furnace wall temperature, while the purge gas velocity and gas type have only minor effects. Xue et al. [40] modeled the transient heat transfer through an eight-hole MOF and found that a MOF heats up faster than a solid one, as there is less material to heat. In addition, the inclusion of radiative heat transfer across the holes accelerates the heating in the whole fibre. However, numerical treatment of the full heat transfer problem requires significant computational efforts, even for the two-dimensional case of a solid fibre where axis symmetry can be exploited to simplify the problem.

In this work, we derive an asymptotic energy equation for the drawing process of annular capillaries by extending the work of Taroni et al. [24] and build a complete asymptotic fibre drawing model with the equations obtained by Fitt et al. [19]. In addition, we include the effects of viscous dissipation in our model. This simplified system of equations can be solved numerically quite readily compared to the full three-dimensional problem, and its predictions are in very good agreement with the experimental results by Luzi et al. [20]. The rest of this manuscript is organized as follows. In Section 2, we develop the theoretical formulation of the problem, concisely yet comprehensively providing the mass, momentum, and energy equations with the associated boundary conditions that govern the drawing process of an annular capillary. In Section 3, we derive the final asymptotic equations for the drawing process of a capillary, unifying the mass, momentum, and evolution equations of Fitt et al. [19] with a simplified energy equation. In Section 4, we compare the numerical outcomes of the asymptotic model with the experimental results of Luzi et al. [20], and in Section 5 we discuss our results, highlighting possible ways to improve the present model. Finally, in Appendix A, we derive an asymptotic energy equation for rotating capillaries and show how it can be coupled with the asymptotic model of Voyce et al. [21].

2. Problem Description

2.1. Governing Equations

A fibre preform is slowly inserted from the top of a furnace through an opening iris and is pulled from the bottom. During drawing, the size of the preform is significantly reduced, and it achieves the required final dimensions at the exit of the furnace. The process is schematically depicted in Figure 1. To develop a suitable mathematical model for describing the fibre drawing process, we begin our study with the full three-dimensional continuity, momentum, and energy equations written in cylindrical coordinates.

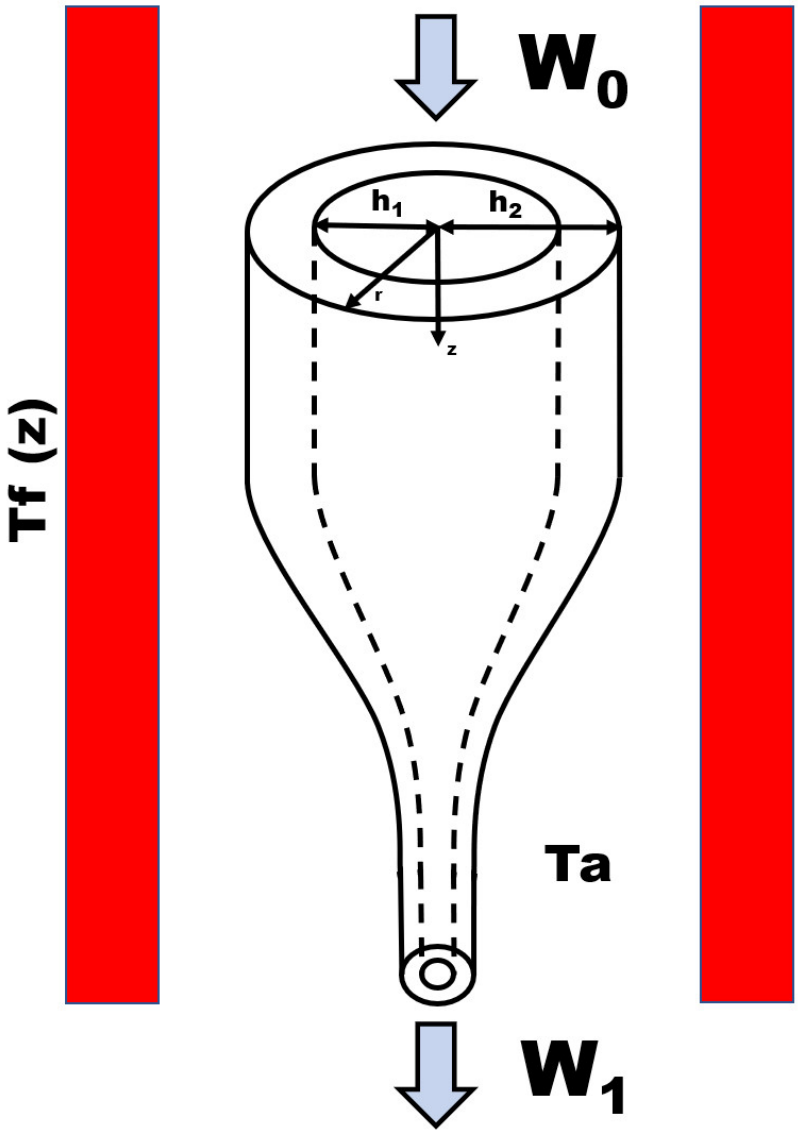


Figure 1. Schematic diagram of the drawing process of an optical glass capillary. The furnace temperature depends on the axial position z, and is indicated by T_f, while the furnace ambient temperature is indicated by T_a.

2.1.1. Mass and Momentum Equations

The continuity and momentum equations in cylindrical coordinates read [41]

$$\frac{\partial \rho}{\partial t} + \frac{1}{r}\frac{(\rho r u)}{\partial r} + \frac{1}{r}\frac{\partial(\rho v)}{\partial \phi} + \frac{\partial(\rho w)}{\partial z} = 0 \tag{1}$$

$$\rho\left(\frac{\partial u}{\partial t} + u\frac{\partial u}{\partial r} + \frac{v}{r}\frac{\partial u}{\partial \phi} - \frac{u^2}{r} + w\frac{\partial u}{\partial z}\right) = f_r - \frac{\partial p}{\partial r} + \frac{1}{r}\frac{\partial(r\tau_{rr})}{\partial r} + \frac{1}{r}\frac{\partial(r\tau_{r\phi})}{\partial \phi} + \frac{\partial(\tau_{rz})}{\partial z} - \frac{\tau_{\phi\phi}}{r} \tag{2}$$

$$\rho\left(\frac{\partial v}{\partial t} + u\frac{\partial v}{\partial r} + \frac{v}{r}\frac{\partial v}{\partial \phi} + \frac{uv}{r} + w\frac{\partial v}{\partial z}\right) = f_\phi - \frac{1}{r}\frac{\partial p}{\partial \phi} + \frac{1}{r^2}\frac{\partial(r^2\tau_{r\phi})}{\partial r} + \frac{1}{r}\frac{\partial(\tau_{\phi\phi})}{\partial \phi} + \frac{\partial(\tau_{\phi z})}{\partial z} \tag{3}$$

$$\rho\left(\frac{\partial w}{\partial t}+u\frac{\partial w}{\partial r}+\frac{v}{r}\frac{\partial w}{\partial \phi}+w\frac{\partial w}{\partial z}\right)=f_z-\frac{\partial p}{\partial z}+\frac{1}{r}\frac{\partial(r\tau_{rz})}{\partial r}+\frac{1}{r}\frac{\partial(r\tau_{\phi z})}{\partial \phi}+\frac{\partial(\tau_{zz})}{\partial z} \tag{4}$$

Herein, ρ, t, and p denote the density, the time, and the pressure, respectively, and r, z, and ϕ represents the radial, axial, and azimuthal coordinates. The fluid velocity is denoted by $\boldsymbol{q}=w\boldsymbol{e}_z+u\boldsymbol{e}_r+v\boldsymbol{e}_\phi$, and $\boldsymbol{e}_z$, $\boldsymbol{e}_r$, and $\boldsymbol{e}_\phi$ are the unit vectors in the axial, radial, and azimuthal directions, respectively. u, v, and w are the radial, azimuthal, and axial components of the velocity field, and $\boldsymbol{f}=f_z\boldsymbol{e}_z+f_r\boldsymbol{e}_r+f_\phi\boldsymbol{e}_\phi=\rho g(\boldsymbol{e}_z+\boldsymbol{e}_r+\boldsymbol{e}_\phi)$ represents the body force. The components of the viscous stress tensor read

$$\tau_{rr}=\mu\left(2\frac{\partial u}{\partial r}-\frac{2}{3}(\boldsymbol{\nabla}\cdot\boldsymbol{q})\right)$$

$$\tau_{\phi\phi}=\mu\left(2\left(\frac{1}{r}\frac{\partial v}{\partial \phi}+\frac{u}{r}\right)-\frac{2}{3}(\boldsymbol{\nabla}\cdot\boldsymbol{q})\right)$$

$$\tau_{zz}=\mu\left(2\frac{\partial w}{\partial z}-\frac{2}{3}(\boldsymbol{\nabla}\cdot\boldsymbol{q})\right)$$

$$\tau_{r\phi}=\mu\left(r\frac{\partial}{\partial r}\left(\frac{v}{r}\right)+\frac{1}{r}\frac{\partial u}{\partial \phi}\right)$$

$$\tau_{rz}=\mu\left(\frac{\partial w}{\partial r}+\frac{\partial u}{\partial z}\right)$$

$$\tau_{\phi z}=\mu\left(\frac{\partial v}{\partial z}+\frac{1}{r}\frac{\partial w}{\partial \phi}\right)$$

The divergence of the velocity field may be written as

$$\boldsymbol{\nabla}\cdot\boldsymbol{q}=\frac{1}{r}\frac{\partial(ru)}{\partial r}+\frac{1}{r}\frac{\partial v}{\partial \phi}+\frac{\partial w}{\partial z} \tag{5}$$

The left-hand side of the momentum equations denotes the temporal and convective inertial acceleration, while the right-hand side incorporates the pressure gradient, divergence of the stress tensor, and sum of the body forces.

2.1.2. Two-Dimensional Mass and Momentum Equations

We assume the flow to be incompressible, and consider axis symmetry and a non-rotating capillary, say, $\rho=const$, $\frac{\partial}{\partial \phi}=0$, and $v=0$. Therefore, the mass conservation equation reduces to

$$\frac{1}{r}\frac{\partial(ru)}{\partial r}+\frac{\partial w}{\partial z}=0 \tag{6}$$

and many terms of the components of the stress tensor vanish:

$$\tau_{rr}=2\mu\left(\frac{\partial u}{\partial r}\right)$$

$$\tau_{\phi\phi}=2\mu\left(\frac{u}{r}\right)$$

$$\tau_{zz}=2\mu\left(\frac{\partial w}{\partial z}\right)$$

$$\tau_{r\phi}=0$$

$$\tau_{rz} = \mu\left(\frac{\partial w}{\partial r} + \frac{\partial u}{\partial z}\right)$$
$$\tau_{\phi z} = 0$$

Thereby, the previous momentum equations reduce to

$$\begin{aligned}\rho\left(\frac{\partial u}{\partial t} + u\frac{\partial u}{\partial r} + w\frac{\partial u}{\partial z}\right) &= f_r - \frac{\partial p}{\partial r} \\ +\frac{2}{r}\frac{\partial}{\partial r}\left(r\mu\left(\frac{\partial u}{\partial r}\right)\right) + \frac{\partial}{\partial z}\left(\mu\left(\frac{\partial w}{\partial r} + \frac{\partial u}{\partial z}\right)\right) &- 2\mu\frac{u}{r^2}\end{aligned} \tag{7}$$

$$\begin{aligned}\rho\left(\frac{\partial w}{\partial t} + u\frac{\partial w}{\partial r} + w\frac{\partial w}{\partial z}\right) &= f_z - \frac{\partial p}{\partial z} + \frac{1}{r}\frac{\partial}{\partial r}\left(r\mu\left(\frac{\partial w}{\partial r} + \frac{\partial u}{\partial z}\right)\right) \\ &+2\frac{\partial}{\partial z}\left(\mu\frac{\partial w}{\partial z}\right)\end{aligned} \tag{8}$$

because the momentum equation in the azimuthal direction vanishes identically. To close the problem, boundary and initial conditions must be specified. Concerning boundary conditions, we impose initial, kinematic, and dynamic boundary conditions. The kinematic boundary conditions require that the normal components of the velocity at each interface of the capillary be continuous across the interfaces. In addition, the tangential component of the velocity must be continuous at the interfaces. At each fibre surface, they read

$$\frac{\partial h_1}{\partial t} + w\frac{\partial h_1}{\partial z} = u \tag{9a}$$

$$\frac{\partial h_2}{\partial t} + w\frac{\partial h_2}{\partial z} = u \tag{9b}$$

The normal boundary conditions represent a balance of forces across the surfaces of the capillary. They may be written as

$$-\boldsymbol{n}_1^T \cdot \boldsymbol{\tau} \cdot \boldsymbol{n}_1 + \frac{\gamma}{h_1} = p_H \tag{10a}$$

$$-\boldsymbol{n}_2^T \cdot \boldsymbol{\tau} \cdot \boldsymbol{n}_2 - \frac{\gamma}{h_2} = p_a \tag{10b}$$

in the normal direction, and

$$\boldsymbol{t}_1^T \cdot \boldsymbol{\tau} \cdot \boldsymbol{n}_1 = 0 \tag{10c}$$

$$\boldsymbol{t}_2^T \cdot \boldsymbol{\tau} \cdot \boldsymbol{n}_2 = 0 \tag{10d}$$

in the tangential direction. In Equation (10), $\boldsymbol{\tau}$, $\boldsymbol{t}$, and $\boldsymbol{n}$ denote the stress tensor and the unit vectors in the tangential and normal directions, respectively. They read

$$\boldsymbol{\tau} = \begin{bmatrix} 2\mu\left(\frac{\partial w}{\partial z}\right) - p & \mu\left(\frac{\partial w}{\partial r} + \frac{\partial u}{\partial z}\right) \\ \mu\left(\frac{\partial w}{\partial r} + \frac{\partial u}{\partial z}\right) & 2\mu\left(\frac{\partial u}{\partial r}\right) - p \end{bmatrix} \tag{11a}$$

$$\boldsymbol{t}_i^T = \frac{(-1)^{i+1}}{\sqrt{1 + \left(\frac{\partial h_i}{\partial z}\right)^2}}\left(1\boldsymbol{e}_z + \frac{\partial h_i}{\partial z}\boldsymbol{e}_r\right) \tag{11b}$$

$$\boldsymbol{n}_i^T = \frac{(-1)^{i+1}}{\sqrt{1 + \left(\frac{\partial h_i}{\partial z}\right)^2}}\left(\frac{\partial h_i}{\partial z}\boldsymbol{e}_z - 1\boldsymbol{e}_r\right) \tag{11c}$$

Moreover, γ, p_H, and p_a are the surface tension, the hole, and the ambient pressure, respectively. To close the problem, we impose the velocity at the beginning and end of the drawing process as initial conditions:

$$w(t,r,z=0)=W_0, \qquad w(t,r,z=L)=W_1 \tag{11d}$$

2.1.3. Energy Equation

The three-dimensional energy equation in cylindrical coordinates assumes the form

$$\begin{aligned}\rho c_p\left(\frac{\partial T}{\partial t}+u\frac{\partial T}{\partial r}+\frac{v}{r}\frac{\partial T}{\partial \phi}+w\frac{\partial T}{\partial z}\right)&=\frac{1}{r}\frac{\partial}{\partial r}\left(kr\frac{\partial T}{\partial r}\right)\\ +\frac{1}{r}\frac{\partial}{\partial \phi}\left(\frac{k}{r}\frac{\partial T}{\partial \phi}\right)+\frac{\partial}{\partial z}\left(k\frac{\partial T}{\partial z}\right)+\beta T\left(\frac{\partial p}{\partial t}+u\frac{\partial p}{\partial r}+\frac{v}{r}\frac{\partial p}{\partial \phi}+w\frac{\partial p}{\partial z}\right)+\Phi\end{aligned} \tag{12}$$

In Equation (12), k and c_p denote the thermal conductivity and the specific heat capacity. In addition, T, β, and Φ are the temperature, the coefficient of thermal expansion at constant pressure, and the viscous dissipation, respectively. The viscous dissipation Φ reads

$$\begin{aligned}\frac{\Phi}{\mu}=2\left[\left(\frac{\partial u}{\partial r}\right)^2+\left(\frac{1}{r}\frac{\partial v}{\partial \phi}+\frac{u}{r}\right)^2+\left(\frac{\partial w}{\partial z}\right)^2\right]+\left[\frac{1}{r}\frac{\partial w}{\partial \phi}+\frac{\partial v}{\partial z}\right]^2\\ +\left[r\frac{\partial}{\partial r}\left(\frac{v}{r}\right)+\frac{1}{r}\frac{\partial u}{\partial \phi}\right]^2+\left[\frac{\partial u}{\partial z}+\frac{\partial w}{\partial r}\right]^2-\frac{2}{3}(\boldsymbol{\nabla}\cdot\boldsymbol{q})\end{aligned} \tag{13}$$

Assuming axis symmetry and constant density, Equation (12) reduces to

$$\begin{aligned}\rho c_p\left(\frac{\partial T}{\partial t}+u\frac{\partial T}{\partial r}+w\frac{\partial T}{\partial z}\right)&=\frac{1}{r}\frac{\partial}{\partial r}\left(kr\frac{\partial T}{\partial r}\right)+\frac{\partial}{\partial z}\left(k\frac{\partial T}{\partial z}\right)\\ +2\mu\left[\left(\frac{\partial u}{\partial r}\right)^2+\left(\frac{u}{r}\right)^2+\left(\frac{\partial w}{\partial z}\right)^2\right]+\mu\left[\frac{\partial u}{\partial z}+\frac{\partial w}{\partial r}\right]^2\end{aligned} \tag{14}$$

The left-hand side of the energy equation denotes the change of temperature with time and thermal convection. The right-hand side encompasses thermal conduction and viscous dissipation. Because glass is a transparent material, radiative heat transfer within the fibre is relevant, especially at high temperatures. Nevertheless, we avoid the full description of the problem in detail and opt for the common approximation in which the capillary is optically thick. Thereby, we assume that the capillary thickness is much greater than the absorption length scale. Following Taroni et al. [24], we utilize the Rosseland approximation and add a radiative contribution to the total thermal conductivity, say, $k(T)=k_c+k_r(T)$

$$k_r(T)=\frac{16n_0^2\sigma T^3}{3\chi} \tag{15}$$

where n_0 and χ are the refractive index and the absorption coefficient, respectively. Therefore, Equation (14) assumes the form

$$\begin{aligned}\rho c_p\left(\frac{\partial T}{\partial t}+u\frac{\partial T}{\partial r}+w\frac{\partial T}{\partial z}\right)&=\frac{1}{r}\frac{\partial}{\partial r}\left(k_c r\frac{\partial T}{\partial r}\right)\\ +\frac{1}{r}\frac{\partial}{\partial r}\left(\tilde{k}_r r\frac{\partial T^4}{\partial r}\right)+\frac{\partial}{\partial z}\left(k_c\frac{\partial T}{\partial z}\right)+\frac{\partial}{\partial z}\left(\tilde{k}_r\frac{\partial T^4}{\partial z}\right)\\ +2\mu\left[\left(\frac{\partial u}{\partial r}\right)^2+\left(\frac{u}{r}\right)^2+\left(\frac{\partial w}{\partial z}\right)^2\right]+\mu\left[\frac{\partial u}{\partial z}+\frac{\partial w}{\partial r}\right]^2\end{aligned} \tag{16}$$

where $\tilde{k}_r = \frac{k_r(T)}{4T^3}$. The thermal boundary conditions at the outer glass-air interface read

$$-k\frac{\partial T}{\partial r} = \sigma\epsilon_r\left(T^4 - T_f^4\right) + k_h(T - T_a) \tag{17}$$

where σ and ϵ_r are the Stefan-Boltzmann constant and the specific emissivity of the furnace. In addition, k_h, T_f, and T_a are the convective heat exchange coefficient, the furnace, and the ambient temperature, respectively. The boundary condition at the inner surface assumes the form

$$-k\frac{\partial T}{\partial r} = k_h(T - T_a) \tag{18}$$

Finally, we impose the temperature at the beginning of the drawing by numerically solving Equation (17) with the left-hand side set equal to zero and specified functional forms of the furnace and ambient temperature.

2.1.4. Non-Dimensionalization

We non-dimensionalize the previous equations by exploiting the slenderness of the geometry, that is, utilizing the ratio $\epsilon = \frac{h_{20}-h_{10}}{L} << 1$, where L is a "hot-zone" length and $h_{20} - h_{10}$ is the initial size of a capillary. We set

$$\begin{array}{lll} r = \epsilon L\bar{r} & z = L\bar{z} & u = \epsilon W_1\overline{u} \\ w = W_1\overline{w} & h_1 = \epsilon L\bar{h}_1 & h_2 = \epsilon L\bar{h}_2 \\ p = \dfrac{\mu_s W_1}{\epsilon^2 L}\overline{p} & T = T_s\overline{T} & t = \dfrac{L}{W_1}\bar{t} \end{array}$$

where overbars indicate non-dimensional quantities, W_1 is a typical draw speed, and T_s and μ_s are typical glass softening temperature and viscosity at the glass softening temperature, respectively. The continuity equation becomes

$$\frac{1}{\overline{r}}\frac{\partial(\overline{r}\,\overline{u})}{\partial\overline{r}} + \frac{\partial\overline{w}}{\partial\overline{z}} = 0 \tag{19}$$

The momentum equation in the z direction reads

$$\begin{aligned} \epsilon^2 Re\left(\frac{\partial\overline{w}}{\partial\overline{t}} + \overline{u}\frac{\partial\overline{w}}{\partial\overline{r}} + \overline{w}\frac{\partial\overline{w}}{\partial\overline{z}}\right) = \epsilon^2\frac{Re}{Fr^2} - \frac{\partial\overline{p}}{\partial\overline{z}} + \frac{1}{\overline{r}}\frac{\partial}{\partial\overline{r}}\left(\overline{r}\,\overline{\mu}\left(\frac{\partial\overline{w}}{\partial\overline{r}}\right)\right) \\ +\epsilon^2\frac{1}{\overline{r}}\frac{\partial}{\partial\overline{r}}\left(\overline{r}\,\overline{\mu}\left(\frac{\partial\overline{u}}{\partial\overline{z}}\right)\right) + 2\epsilon^2\frac{\partial}{\partial\overline{z}}\left(\overline{\mu}\frac{\partial\overline{w}}{\partial\overline{z}}\right) \end{aligned} \tag{20}$$

while the one in the r direction becomes

$$\begin{aligned} \epsilon^4 Re\left(\frac{\partial\overline{u}}{\partial\overline{t}} + \overline{u}\frac{\partial\overline{u}}{\partial\overline{r}} + \overline{w}\frac{\partial\overline{u}}{\partial\overline{z}}\right) = \epsilon^3\frac{Re}{Fr^2} - \frac{\partial\overline{p}}{\partial\overline{r}} \\ +2\frac{\epsilon^2}{\overline{r}}\frac{\partial}{\partial\overline{r}}\left(\overline{r}\,\overline{\mu}\left(\frac{\partial\overline{u}}{\partial\overline{r}}\right)\right) + \epsilon^2\frac{\partial}{\partial\overline{z}}\left(\overline{\mu}\left(\frac{\partial\overline{w}}{\partial\overline{r}}\right)\right) + \epsilon^4\frac{\partial}{\partial\overline{z}}\left(\overline{\mu}\left(\frac{\partial\overline{u}}{\partial\overline{z}}\right)\right) - 2\epsilon^2\overline{\mu}\left(\frac{\overline{u}}{\overline{r}^2}\right) \end{aligned} \tag{21}$$

where we have set $\mu = \mu_s\overline{\mu}$ and $\boldsymbol{f} = \rho\boldsymbol{g}$. Moreover,

$$Re = \frac{L\rho W_1}{\mu_s}$$
$$Fr = \frac{W_1^2}{\sqrt{Lg}}$$

where Re and Fr are the Reynolds and the Froude numbers, respectively. The energy equation assumes the form

$$\begin{aligned}\epsilon^2 Pe\left(\frac{\partial \overline{T}}{\partial \overline{t}}+\overline{u}\frac{\partial \overline{T}}{\partial \overline{r}}+\overline{w}\frac{\partial \overline{T}}{\partial \overline{z}}\right)&=\frac{1}{\overline{r}}\frac{\partial}{\partial \overline{r}}\left(\overline{r}\frac{\partial \overline{T}}{\partial \overline{r}}\right)+\frac{1}{\overline{r}}\frac{\partial}{\partial \overline{r}}\left(\gamma_R\overline{r}\frac{\partial \overline{T}^4}{\partial \overline{r}}\right)+\epsilon^2\frac{\partial}{\partial \overline{z}}\left(\frac{\partial \overline{T}}{\partial \overline{z}}\right)\\ +\epsilon^2\frac{\partial}{\partial \overline{z}}\left(\gamma_R\frac{\partial \overline{T}^4}{\partial \overline{z}}\right)&+2\epsilon^2 Br\overline{\mu}\left[\left(\frac{\partial \overline{u}}{\partial \overline{r}}\right)^2+\left(\frac{\overline{u}}{\overline{r}}\right)^2+\left(\frac{\partial \overline{w}}{\partial \overline{z}}\right)^2\right]+\epsilon^2 Br\overline{\mu}\left[\frac{\partial \epsilon\overline{u}}{\partial z}+\frac{\partial \overline{w}}{\partial \epsilon\overline{r}}\right]^2\end{aligned} \tag{22}$$

where

$$\begin{aligned}Pe&=\frac{L\rho W_1 c_p}{k_c}\\ Br&=\frac{\mu_s W_1^2}{T_s k_c}\\ \gamma_R&=\frac{4n_0^2\sigma T_s^3}{3\chi k_c}\end{aligned}$$

In the previous equation, Pe and Br are the Peclet and the Brinkman number, respectively. The former denotes the ratio between the convective transport of thermal energy to the fluid to the conduction of thermal energy within the fluid, and the latter is a ratio between the heat originated by mechanical dissipation to the heat transferred by conduction. Furthermore, γ_R is a parameter that indicates the strength of bulk diffusion [24]. The dimensionless kinematic boundary conditions for the inner and the outer surfaces read

$$\frac{\partial \overline{h}_1}{\partial \overline{t}}+\overline{w}\frac{\partial \overline{h}_1}{\partial \overline{z}}=\overline{u} \tag{23a}$$

$$\frac{\partial \overline{h}_2}{\partial \overline{t}}+\overline{w}\frac{\partial \overline{h}_2}{\partial \overline{z}}=\overline{u} \tag{23b}$$

while the dimensionless dynamic boundary conditions in the normal and tangential direction assume the form

$$\begin{aligned}-2\overline{\mu}\epsilon^2\frac{\partial \overline{w}}{\partial \overline{z}}\left(\frac{\partial \overline{h}_1}{\partial \overline{z}}\right)^2+2\overline{\mu}\frac{\partial \overline{h}_1}{\partial \overline{z}}\frac{\partial \overline{w}}{\partial \overline{r}}\Big|_{\overline{r}=\overline{h}_1}+2\epsilon^2\overline{\mu}\frac{\partial \overline{h}_1}{\partial \overline{z}}\frac{\partial \overline{u}}{\partial \overline{z}}\\ -2\overline{\mu}\frac{\partial \overline{u}}{\partial \overline{r}}\Big|_{\overline{r}=\overline{h}_1}+\frac{\overline{\gamma}}{\overline{h}_1}\left(1+\epsilon^2\left(\frac{\partial \overline{h}_1}{\partial \overline{z}}\right)^2\right)\\ =\frac{1}{\epsilon^2}(\overline{p}_H-\overline{p})\left(1+\epsilon^2\left(\frac{\partial \overline{h}_1}{\partial \overline{z}}\right)^2\right)\end{aligned} \tag{24a}$$

$$\begin{aligned}-2\overline{\mu}\epsilon^2\frac{\partial \overline{w}}{\partial \overline{z}}\left(\frac{\partial \overline{h}_2}{\partial \overline{z}}\right)^2+2\overline{\mu}\frac{\partial \overline{h}_2}{\partial \overline{z}}\frac{\partial \overline{w}}{\partial \overline{r}}\Big|_{\overline{r}=\overline{h}_2}+2\epsilon^2\overline{\mu}\frac{\partial \overline{h}_2}{\partial \overline{z}}\frac{\partial \overline{u}}{\partial \overline{z}}\\ -2\overline{\mu}\frac{\partial \overline{u}}{\partial \overline{r}}\Big|_{\overline{r}=\overline{h}_2}-\frac{\overline{\gamma}}{\overline{h}_2}\left(1+\epsilon^2\left(\frac{\partial \overline{h}_2}{\partial \overline{z}}\right)^2\right)\\ =\frac{1}{\epsilon^2}(\overline{p}_a-\overline{p})\left(1+\epsilon^2\left(\frac{\partial \overline{h}_2}{\partial \overline{z}}\right)^2\right)\end{aligned} \tag{24b}$$

$$\begin{aligned}2\overline{\mu}\epsilon\frac{\partial \overline{w}}{\partial \overline{z}}\frac{\partial \overline{h}_1}{\partial \overline{z}}-2\overline{\mu}\epsilon\frac{\partial \overline{h}_1}{\partial \overline{z}}\frac{\partial \overline{u}}{\partial \overline{r}}\Big|_{\overline{r}=\overline{h}_1}\\ +\overline{\mu}\left(\frac{\partial \epsilon\overline{h}_1}{\partial \overline{z}}\right)^2\left(\frac{\partial \overline{w}}{\partial \epsilon\overline{r}}+\frac{\partial \epsilon\overline{u}}{\partial \overline{z}}\right)-\overline{\mu}\left(\frac{\partial \overline{w}}{\partial \epsilon\overline{r}}+\frac{\partial \epsilon\overline{u}}{\partial \overline{z}}\right)=0\end{aligned} \tag{24c}$$

$$2\overline{\mu}\epsilon\frac{\partial\overline{w}}{\partial\overline{z}}\frac{\partial\overline{h}_2}{\partial\overline{z}} - 2\overline{\mu}\epsilon\frac{\partial\overline{h}_2}{\partial\overline{z}}\frac{\partial\overline{u}}{\partial\overline{r}}\bigg|_{\overline{r}=\overline{h}_2}$$
$$+\overline{\mu}\left(\frac{\partial\epsilon\overline{h}_2}{\partial\overline{z}}\right)^2\left(\frac{\partial\overline{w}}{\partial\epsilon\overline{r}}+\frac{\partial\epsilon\overline{u}}{\partial\overline{z}}\right) - \overline{\mu}\left(\frac{\partial\overline{w}}{\partial\epsilon\overline{r}}+\frac{\partial\epsilon\overline{u}}{\partial\overline{z}}\right) = 0 \quad (24d)$$

Finally, the dimensionless thermal boundary conditions for the outer and the inner surface read

$$-\left(1+4\gamma_R\overline{T}^3\frac{\partial\overline{T}}{\partial\overline{r}}\right) = \epsilon\alpha(\overline{T}^4-\overline{T}_f^4)+\epsilon\beta(\overline{T}-\overline{T}_a) \quad (25a)$$

$$-\left(1+4\gamma_R\overline{T}^3\right)\frac{\partial\overline{T}}{\partial\overline{r}} = \epsilon\beta(\overline{T}-\overline{T}_a) \quad (25b)$$

In Equation (25), $\alpha = \frac{\sigma\epsilon_r T_s^3 L}{k_c}$ represents the ratio between the radiative and the conductive heat exchange, while $\beta = \frac{k_h L}{k_c}$ is the Nusselt number, that is, the ratio between convective and conductive heat transfer [24].

2.1.5. Determination of the Furnace and Ambient Temperature Profiles

As our furnace is very similar to the one used by Voyce et al. [22], we begin the determination of the temperature profiles of the furnace by extracting their experimental values. Voyce et al. [22] measured the temperature profile of the oven by inserting a thermocouple into the air hole of a capillary tube that was slowly introduced into the oven, allowing the thermal equilibrium between the fibre and the furnace to be assumed. They measured the temperature profile of the furnace at three peak temperatures, say, 1300 °C, 1600 °C, and 1760 °C, reporting that it is very challenging to measure temperature profiles at peak temperatures higher than 1700 °C as thermocouples become inaccurate and may melt. They measured the temperature distribution only in a restricted portion of the furnace, in the vicinity of the peak value where the temperature is high enough to permit the drawing process to occur. The length of this portion of the oven is approximately 12 mm. We extract the experimental data of Voyce et al. [22] and interpolate them with a functional form similar to the one proposed by Taroni et al. [24]:

$$\overline{T}_f(\overline{z}) = \overline{T}_M\left(\frac{1}{5}+\frac{4}{5}exp\left(c(\overline{T}_M)(\overline{z}-0.5)^2\right)\right) \quad (26)$$

see Figure 2, where $\overline{T}_M = \frac{T_M}{Ts}$ and

$$c(\overline{T}_M) = 2.1053\overline{T}_M - 4.6316 \quad (27)$$

With this selection of the parameters, we keep the temperature distribution centred in the middle of the "hot zone" and let the width of the distribution depend on the peak temperature. Our choice is motivated by the fact that the temperature peaks shift only slightly towards the left with respect to the furnace center when the peak temperature increases. On the other hand, the width of the temperature distribution is affected by the peak temperature. Using Equation (26), we always obtain interpolation curves with $R^2 > 0.9$ for the three temperature distributions measured by Taroni et al. [24]. We accept this result and do not try to obtain a closer match between interpolated and experimental data. In addition, we choose $\overline{T}_a(\overline{z}) = \frac{3}{4}\overline{T}_f$, in accordance with Taroni et al. [24].

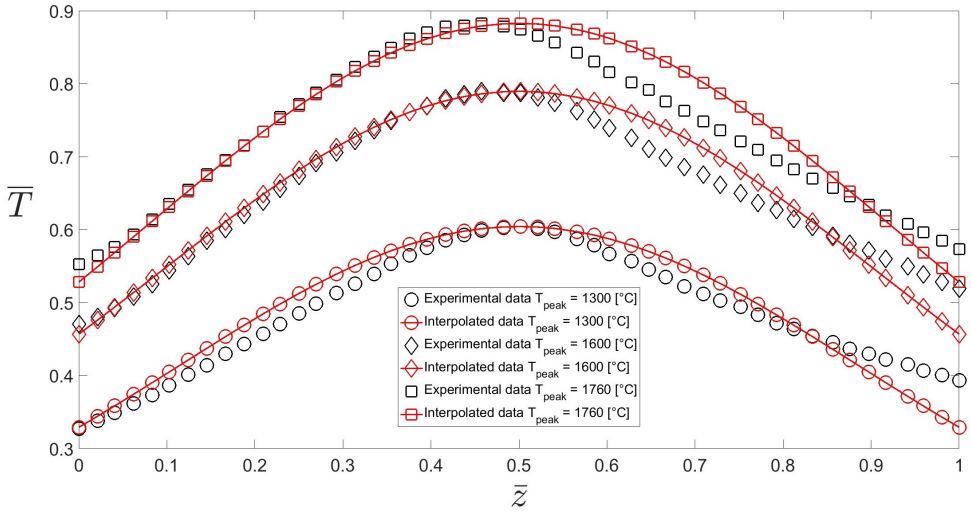


Figure 2. Furnace temperature profiles measured at three different peak temperatures by Voyce et al. [22] and interpolated temperature profiles according to the relation in (26).

2.1.6. The Functional Form of ϵ_r, k_h, α, and β

In general, values of the specific emissivity ϵ_r and the convective heat transfer coefficient k_h depend on fibre thickness, temperature, and properties of the material. Here, we follow the approach of Taroni et al. [24] by selecting

$$\epsilon_r = 1 - e^{-2.5\chi(h_2 - h_1)} \tag{28}$$

where we replace the fibre radius with the capillary thickness. Therefore, the specific emissivity ϵ_r decreases with decreasing capillary thickness. Concerning the convective heat transfer coefficient k_h, we utilize the form suggested by Geyling and Homsy [42]

$$k_h = \frac{w^{\frac{1}{3}}}{(h_2 - h_1)^{\frac{2}{3}}} \tag{29}$$

for the case of slow drawing ratios, while in the case of high drawing ratios we employ the correlation from Patel et al. [43] in the form suggested by Xue et al. [25]

$$k_h = 128.27 w^{0.574} \tag{30}$$

In Equation (29), we consider the capillary thickness instead of the radius. Finally, following the work of Taroni et al. [24], we let α vary with the capillary thickness:

$$\alpha = \frac{\sigma \epsilon_r T_s^3 L}{k_c} \left(1 - e^{-2.5\chi(h_2 - h_1)}\right) \tag{31}$$

However, in contrast to Taroni et al. [24] we utilize variable Nusselt numbers β, with k_h defined by Equations (29) and (30):

$$\beta = \frac{w^{\frac{1}{3}} L}{k_c (h_2 - h_1)^{\frac{2}{3}}} \tag{32}$$

in the case of slow drawing ratios and

$$\beta = \frac{128.27 w^{0.574} L}{k_c} \tag{33}$$

in the case of high drawing ratios.

2.1.7. The Viscosity of Silica Glass

Following Voyce et al. [22], we choose the correlation by Urbain et al. [44] for the viscosity in the temperature range 1400 °C ≤ T ≤ 2500 °C and the one by Hetherington et al. [45] for the temperature range 1000 °C ≤ T ≤ 1400 °C. Urbain et al. [44] utilized the rotating cup technique to measure the viscosity in the interval between 10^{-1} and 10^{5} Poise and the isothermal penetration method to measure the viscosity in the interval between 10^{8} and 10^{13} Poise. Because the isothermal penetration method does not allow a glass metastable equilibrium to be reached, we opt for the correlation provided by Hetherington et al. [45]. They used a fibre elongation technique to measure the viscosity of the silica in this temperature range, checking that the silica was in an equilibrium condition [46]. Therefore, we utilize the following correlation:

$$\mu = 5.8 \cdot 10^{-8} exp\left(\frac{515400}{8.3145T}\right) \tag{34}$$

for the temperature range 1400 °C ≤ T ≤ 2500 °C. Instead, we use

$$\mu = 3.8 \cdot 10^{-14} exp\left(\frac{712000}{8.3145T}\right) \tag{35}$$

for the temperature range 1000 °C < T ≤ 1400 °C. In (34) and (35), the viscosity μ is in $Pa \cdot s$ and the temperature T is in K.

3. Final Asymptotic Equations

Non-Rotating Capillary

We proceed with a regular parameter expansion of the unknowns

$$\begin{aligned}
\overline{w} &= \overline{w}_0(\bar{t}, \bar{z}) + \epsilon^2 \overline{w}_1(\bar{t}, \bar{z}, \bar{r}) \\
\overline{u} &= \overline{u}_0(\bar{t}, \bar{z}, \bar{r}) + \epsilon^2 \overline{u}_1(\bar{t}, \bar{z}, \bar{r}) \\
\overline{p} &= \overline{p}_a + \epsilon^2 \overline{P}(\bar{t}, \bar{z}, \bar{r}) \\
\overline{T} &= \overline{T}_0(\bar{t}, \bar{z}, \bar{r}) + \epsilon^2 \overline{T}_1(\bar{t}, \bar{z}, \bar{r})
\end{aligned}$$

and utilize it in the previously derived non-dimensional mass conservation (Equation (19)), momentum (Equations (20) and (21)), and energy equations (Equation (22)) and boundary conditions (Equations (23) and (24)). By retaining the terms of the expansion at most up to order ϵ^2, we can obtain the equations of Fitt et al. [19]:

$$\frac{\partial(\overline{h}_1^2 \overline{w}_0)}{\partial \bar{z}} = \frac{\overline{p}_0 \overline{h}_2^2 \overline{h}_1^2 - \overline{\gamma} \overline{h}_2 \overline{h}_1 (\overline{h}_2 + \overline{h}_1)}{\mu(\overline{h}_2^2 - \overline{h}_1^2)} \tag{36}$$

$$\frac{\partial(\overline{h}_2^2 \overline{w}_0)}{\partial \bar{z}} = \frac{\overline{p}_0 \overline{h}_2^2 \overline{h}_1^2 - \overline{\gamma} \overline{h}_2 \overline{h}_1 (\overline{h}_2 + \overline{h}_1)}{\mu(\overline{h}_2^2 - \overline{h}_1^2)} \tag{37}$$

$$\frac{\partial}{\partial \bar{z}}\left(3\overline{\mu}\frac{\partial \overline{w}_0}{\partial \bar{z}}(\overline{h}_2^2 - \overline{h}_1^2) + \overline{\gamma}(\overline{h}_2 + \overline{h}_1)\right) = 0 \tag{38}$$

These are evolution equations for the inner and outer fibre surface and an axial momentum equation; for more details see [19]. In Equation (38), we have neglected the inertia terms due to the small values that the Reynolds number Re typically assumes; as a matter of fact, $Re \approx 10^{-8}$ [29]. With regard to the energy equation, we consider the case at the leading order, where $Pe = \frac{\widetilde{P}}{\epsilon^2}$ and $Br = \frac{\widetilde{Br}}{\epsilon^2}$:

$$\begin{aligned}\widetilde{P}\left(\frac{\partial\overline{T}}{\partial\overline{t}}+\overline{u}\frac{\partial\overline{T}}{\partial\overline{r}}+\overline{w}\frac{\partial\overline{T}}{\partial\overline{z}}\right)&=\frac{1}{\overline{r}}\frac{\partial}{\partial\overline{r}}\left(\overline{r}\frac{\partial\overline{T}}{\partial\overline{r}}\right)+\frac{1}{\overline{r}}\frac{\partial}{\partial\overline{r}}\left(\gamma_R\overline{r}\frac{\partial\overline{T}^4}{\partial\overline{r}}\right)\\&+2\widetilde{Br}\overline{\mu}\left[\left(\frac{\partial\overline{u}}{\partial\overline{r}}\right)^2+\left(\frac{\overline{u}}{\overline{r}}\right)^2+\left(\frac{\partial\overline{w}}{\partial\overline{z}}\right)^2\right]+\widetilde{Br}\overline{\mu}\left[\frac{\partial\epsilon\overline{u}}{\partial z}+\frac{\partial\overline{w}}{\partial\epsilon\overline{r}}\right]^2\end{aligned}\tag{39}$$

This case corresponds to the general situation, where the convective heat transport balances the heat transfer across the fibre and the viscous dissipation [24]. Following Taroni et al. [24], we change variables to a more convenient coordinate frame that suits the geometry of the capillary:

$$\overline{x}(\overline{r},\overline{z})=\frac{\overline{r}-\overline{h}_1(\overline{z})}{\overline{h}_2(\overline{z})-\overline{h}_1(\overline{z})}\rightarrow\overline{r}=\overline{x}(\overline{h}_2-\overline{h}_1)+\overline{h}_1,\qquad\overline{\zeta}=\overline{z}\tag{40}$$

The continuity in Equation (19) at the leading order becomes

$$\overline{u}_0=-\frac{\partial\overline{w}_0}{\partial\overline{\zeta}}\frac{[\overline{x}(\overline{h}_2-\overline{h}_1)+\overline{h}_1]}{2}+\frac{\overline{A}(\overline{\zeta})}{[\overline{x}(\overline{h}_2-\overline{h}_1)+\overline{h}_1]}\tag{41}$$

where $\overline{A}$ is

$$\overline{A}=\frac{\overline{p}_0\overline{h}_2^2\overline{h}_1^2-\overline{\gamma}\overline{h}_2\overline{h}_1(\overline{h}_2+\overline{h}_1)}{2\overline{\mu}(\overline{h}_2^2-\overline{h}_1^2)}\tag{42}$$

and the axial momentum equation after being integrated once with respect to $\overline{z}$ assumes the form

$$\frac{\partial\overline{w}_0}{\partial\overline{\zeta}}=\left(\frac{\overline{F}-\overline{\gamma}(\overline{h}_2+\overline{h}_1)}{3\overline{\mu}(\overline{h}_{20}^2-\overline{h}_{10}^2)\overline{W}_0}\right)\overline{w}_0\tag{43}$$

where the constant $\overline{F}$ arising from the integration physically represents the tension needed to pull the fibre. In addition, the following identity

$$\overline{h}_2^2-\overline{h}_1^2=\frac{(\overline{h}_{20}^2-\overline{h}_{10}^2)\overline{W}_0}{\overline{w}_0}\tag{44}$$

has been used, and represents an equation of mass conservation. We now change the variables in Equation (39) according to Equation (40) and utilize the asymptotic expansions previously defined to obtain

$$\begin{aligned}\frac{\partial\overline{T}}{\partial\overline{\zeta}}&=\overline{\Psi}\frac{\partial\overline{T}_0}{\partial\overline{x}}+\overline{\Omega}\left(\frac{\partial^2\overline{T}_0}{\partial\overline{x}^2}\right)+\overline{\Lambda}\left(\frac{\partial\overline{T}_0}{\partial\overline{x}}\right)^2\\&+\frac{\widetilde{Br}\overline{\mu}}{\overline{w}_0}\left[3\left(\frac{\partial\overline{w}_0}{\partial\overline{\zeta}}\right)^2+\left(\frac{2\overline{A}}{\overline{\Theta}^2}\right)^2\right]\end{aligned}\tag{45}$$

where

$$\overline{\Pi} = [\overline{x}(\overline{h}_2 - \overline{h}_1) + \overline{h}_1](\overline{h}_2 - \overline{h}_1)$$
$$\overline{\Theta} = [\overline{x}(\overline{h}_2 - \overline{h}_1) + \overline{h}_1]$$
$$\overline{\Lambda} = \frac{12\gamma_R \overline{T}_0^2}{\overline{w}_0(\overline{h}_2 - \overline{h}_1)^2}$$
$$\overline{\Omega} = \frac{1 + 4\gamma_R \overline{T}_0^3}{\overline{w}_0(\overline{h}_2 - \overline{h}_1)^2}$$
$$\overline{\Psi} = \frac{1}{\overline{w}_0}\left[\frac{1 + 4\gamma_R \overline{T}_0^3}{\overline{\Pi}} - \frac{\overline{A}}{\overline{\Pi}} + \widetilde{P}\frac{\partial \overline{w}_0}{\partial \overline{\zeta}}\frac{\overline{\Theta}}{2(\overline{h}_2 - \overline{h}_1)}\right]$$

The thermal boundary conditions in Equation (25) at $\overline{r} = \overline{h}_2$ and at $\overline{r} = \overline{h}_1$ become

$$\left.\frac{\partial \overline{T}_0}{\partial \overline{x}}\right|_{\overline{x}=1} = \left[-\frac{\epsilon\alpha(\overline{T}_0^4 - \overline{T}_f^4) + \epsilon\beta(\overline{T}_0 - \overline{T}_a)}{1 + 4\gamma_R \overline{T}_0^3}\right](\overline{h}_2 - \overline{h}_1) \tag{46a}$$

$$\left.\frac{\partial \overline{T}_0}{\partial \overline{x}}\right|_{\overline{x}=0} = -\frac{\epsilon\beta(\overline{T}_0 - \overline{T}_a)}{1 + 4\gamma_R \overline{T}_0^3}(\overline{h}_2 - \overline{h}_1) \tag{46b}$$

4. Results

4.1. Solution Method

We numerically solve the system of differential Equations (36), (37), (43) and (45) using a fourth-order Runge–Kutta–Merson method to integrate them in the axial direction. To this end, we first integrate Equation (43) and iteratively solve the whole system of equations until we find a value of the tension that satisfies the condition

$$\overline{w}_0(\overline{\zeta} = 1) - 1 < 10^{-3}$$

In addition, we discretize Equation (45) and the boundary conditions (46) in the radial direction using second order central difference schemes for both the first and the second derivatives.

All the relevant parameters and initial values for the different cases utilized in the numerical simulations are listed in Table 1. Although the values of the material parameters vary with the temperature, we assumed them to be constant, as their dependence on the temperature is weak. We only let the viscosity vary with the temperature, as its value changes by different orders of magnitude in the temperature range of interest. The step sizes in the axial and radial directions were chosen after a grid study to ensure that the results were trustworthy. We set $\Delta\zeta = 6.25 \times 10^{-7}$ and $\Delta x = 0.2$ for the case of the slow drawing ratios DR36-1, DR54-15, and DR72-2. In the case of the high drawing ratio DR1-102, we utilized $\Delta\zeta = 1.5625 \times 10^{-7}$ and $\Delta x = 0.5$.

Table 1. Main parameters and initial values used for the simulations. [a] Voyce et al. [22], [b] Lee and Yaluria [36], [c] Paek and runk [16], [d] Taroni et al. [24], [e] Huang et al. [47], [f] Myers [17], [g] Fitt et al. [19], [h] Luzi et al. [20].

Parameter	Symbol	Value	Units
Hot zone length [a]	L	0.12	m
Stefan-Boltzmann constant [b]	σ	5.67×10^{-8}	W m^{-2} K^{-4}
Refractive index [b]	n_0	1.5	-
Absorption coefficient [c]	χ	200	m^{-1}
Density [c]	ρ	2200	kg m^{-3}
Specific heat [c]	c_p	1000	J kg^{-1} K^{-1}
Thermal conductivity [d,e]	k_c	1.1	W m^{-1} K^{-1}
Glass softening temperature [f]	T_s	1900	K
Surface tension [g]	γ	0.25	N m^{-1}
Initial external radius [h]	h_{20}	1×10^{-2}	m
Initial internal radius [h]	h_{10}	3.65×10^{-3}	m
Drawing ratio	DR36-1		
Feed speed [h]	W_0	6×10^{-5}	m s^{-1}
Draw speed [h]	W_1	1.67×10^{-2}	m s^{-1}
Drawing ratio	DR54-15		
Feed speed [h]	W_0	9×10^{-5}	m s^{-1}
Draw speed [h]	W_1	2.5×10^{-2}	m s^{-1}
Drawing ratio	DR72-2		
Feed speed [h]	W_0	1.2×10^{-4}	m s^{-1}
Draw speed [h]	W_1	3.33×10^{-2}	m s^{-1}
Drawing ratio	DR1-102		
Feed speed [h]	W_0	1.67×10^{-5}	m s^{-1}
Draw speed [h]	W_1	1.7×10^{-1}	m s^{-1}

4.2. Slow Drawing Ratios

In this section, we first show representative results obtained by solving the system of Equations (36), (37), (43) and (45) for the case DR54-15. Figure 3a shows that the axial velocity profile assumes values close to zero at the beginning of drawing until $\bar{z} \approx 0.4$. Afterwards, it varies abruptly and suddenly increases, reaching the final value of one at $\bar{z} \approx 0.8$. To satisfy the mass conservation equation, the inner and outer surfaces greatly reduce their size before reaching the final dimensions; see Figure 3b. The radii significantly change their sizes and the axial velocity steeply increases only in a small portion of the furnace length measured by Voyce et al. [22]. They termed this part of the oven "hot zone", where the viscosity is low enough to enable the glass to deform. In Figure 3c, we contrast the evolution of the temperature profiles of the inner and outer surfaces of the capillary with that of the furnace along the drawing direction. At the beginning of the drawing, where the speed of the internal and the external surfaces of the capillary are very close to the feed speed, the temperature profiles of the glass surfaces are very close to the temperature distribution of the furnace, indicating thermal equilibrium between the furnace and the capillary. Starting from approximately $\bar{z} \approx 0.5$, the temperature profiles of the capillary surfaces deviate from that of the furnace, resulting in lower values of the glass temperature. Two possible causes lie in the reduced radiative heat exchange between the furnace and the fibre due to the smaller surface and in the significant increase of the convective heat exchange due to the higher values the capillary speed achieves toward the end of the drawing. Furthermore, we observe that the differences between the temperature profiles of the inner and outer radii of the capillary are negligible (see Figure 3c), indicating strong heat diffusion inside the glass due to the radiative contribution to the thermal conductivity. This is clear from the temperature contour displayed in Figure 4, which

shows a substantial axial temperature variation across the fibre length and an imperceptible temperature change in the whole radial direction. In Figure 5, we can compare the final external diameters of the capillaries computed by numerically solving Equations (36), (37), (43) and (45) with the ones obtained experimentally by Luzi et al. [20] for the case of three slow drawing ratios without internal pressurization, that is, DR 36-1, DR 54-15, and DR 72-2, as reported in Table 1. In Figure 6, we compare their final air-filling fractions, that is, the ratio of their final internal radii h_{1f} over their final external radii h_{2f}. By doing this, we vary the peak temperature from 1850 °C up to 2050 °C in steps of 25 °C. The values of both the outer and inner final radii at the end of the drawing process gradually increase with decreasing furnace peak temperature for all three drawing ratios, as the higher viscosity at lower temperatures values hinders the capillary from further decreasing its size. With regard to the final external diameter, the numerical and experimental results are in excellent agreement, with a difference ranging from a minimum of approximately 0.06% up to a maximum of approximately 2%. With regard to the final air-filling fractions of the capillaries, the agreement between the numerical simulations and experimental results is excellent only in the temperature range between 1850 °C and 1975 °C, with a maximum difference of approximately only 2.8%. In the temperature range between 2000 °C and 2050 °C, the discrepancy between the numerical and experimental results varies between approximately 5% and 48%. This maximum extreme difference may be due to too low a value of the surface tension used in the simulations, that is, γ = 0.25 N/m. Another reason for the discrepancy may rely on the possible partial collapse of the inner surface of the capillary. The temperature profile may not be accurately described by the functional form provided by Equation (26) in the case of high peak temperatures, as it has been determined by fitting experimental data obtained at lower peak temperatures. This has a direct impact on the collapse of the capillary, as a simple order of magnitude analysis demonstrates that the collapse time of the inner capillary surface depends on both the viscosity and the surface tension of the molten glass [48]. Because the viscosity greatly varies with the temperature, a different temperature correlation may be required to approximate the furnace temperature profile at high peak temperatures. In addition, the insufficient information concerning the dependency of the surface tension with the temperature makes the estimation of the time required for collapse a very challenging task. In Figures 7 and 8 we examine cases with internal pressurization. First, we keep the pressure constant and vary the peak temperature, then we maintain the temperature and vary the internal pressure. In Figure 7a, we compare the final external diameter of the capillary obtained numerically with the experimental data of Luzi et al. [20], while in Figure 7b we compare the final air-filling fractions obtained numerically and experimentally. In both cases, we keep the internal pressure constant at p_o = 9 mbar and vary the peak temperature of the furnace from 1850 °C up to 2050 °C in steps of 25 °C. The numerical data match very well with the experimental data, with the maximum discrepancy between the final external diameters computed numerically and experimentally being approximately 11% in the case of T_{peak} = 2050 °C. We obtain similar agreement for the final external diameters and the final air-filling fractions in the case where we fix the peak temperature at 1950 °C and vary the internal pressure between 0 and 25 mbar; see Figure 8a,b. In this case, the maximum difference between the experimental values and the numerical computations is approximately 8%. The internal pressure counteracts the effects of the surface tension by promoting an enlargement of the inner hole, thereby increasing the size of the internal and external radii. The maximum deviations between the experimental and numerical results are again obtained for high values of the peak temperatures, where major uncertainties concerning the furnace temperature profile and the value of the surface tension and viscosity prevail.

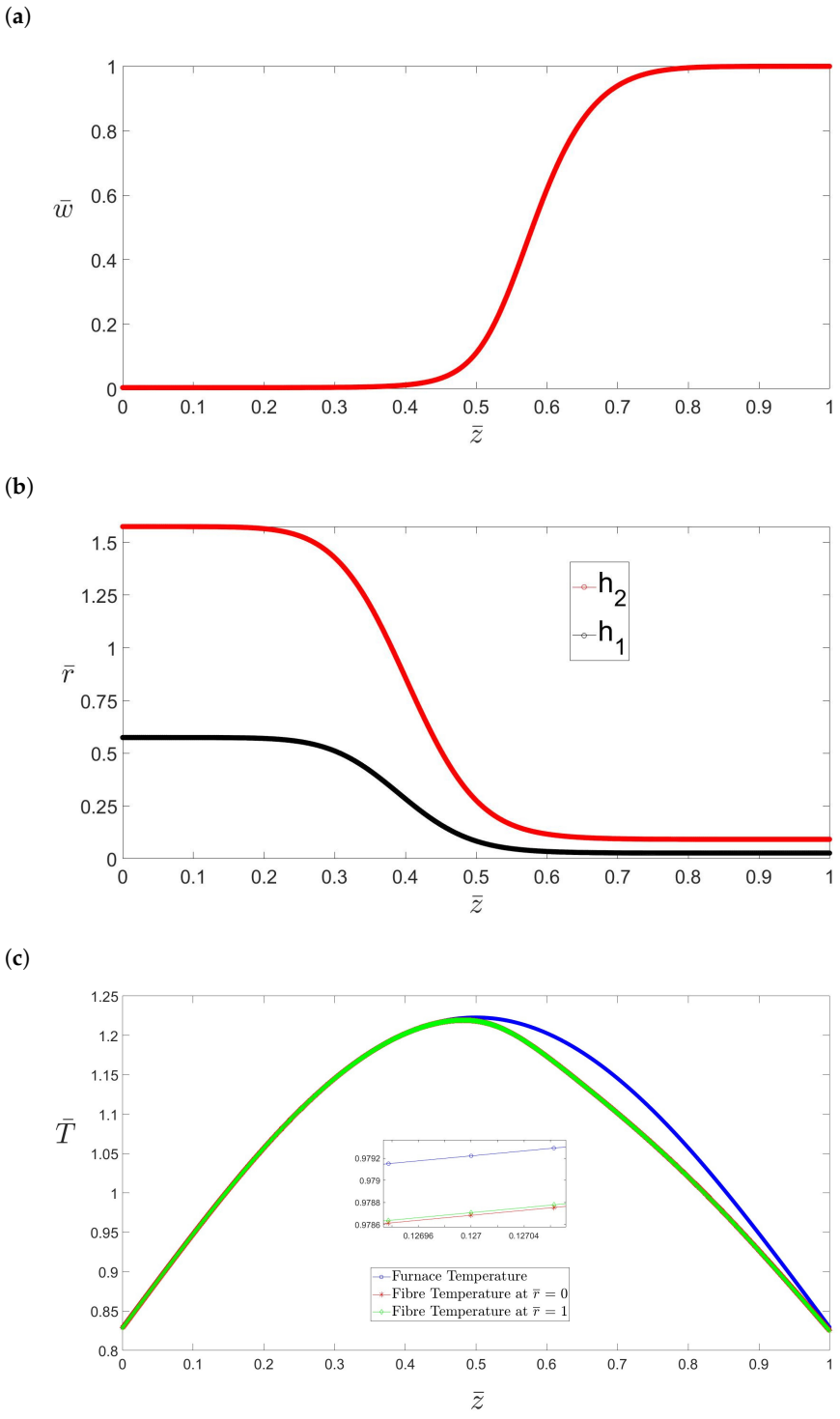


Figure 3. (**a**) Evolution of the axial component of the velocity $\overline{w}$ against the axial distance $\overline{z}$. The inner and outer surfaces of the capillary, $\overline{h}_1$ and $\overline{h}_2$, respectively, are plotted against the axial distance $\overline{z}$ in (**b**). The temperature profiles of the inner and outer capillary surfaces are plotted against the axial distance $\overline{z}$ together with the temperature profile of the furnace in (**c**). The inset in (**c**) magnifies the difference among the plotted temperature profiles of capillary surfaces and the temperature profile of the furnace.

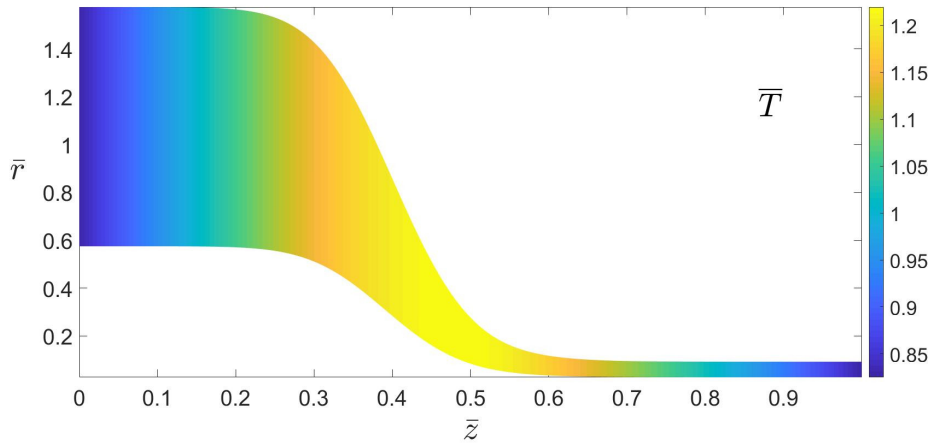
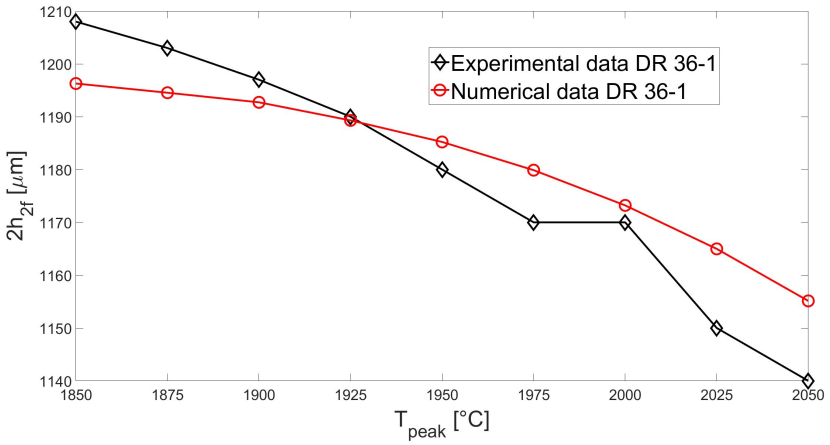


Figure 4. Fibre temperature contour in the case of DR54-15, T_{peak} = 2050 °C and no internal pressurization.

(**a**)



(**b**)

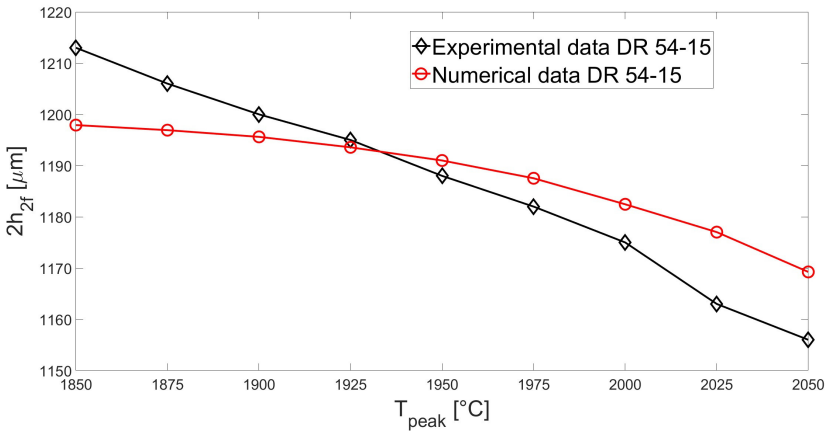


Figure 5. *Cont.*

(**c**)

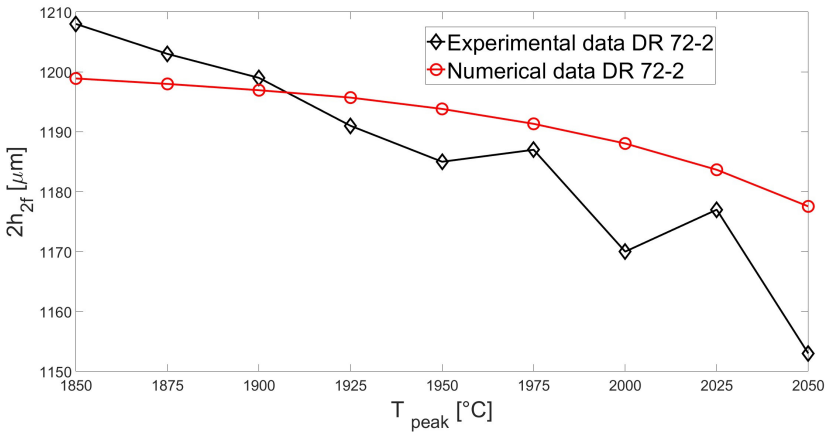
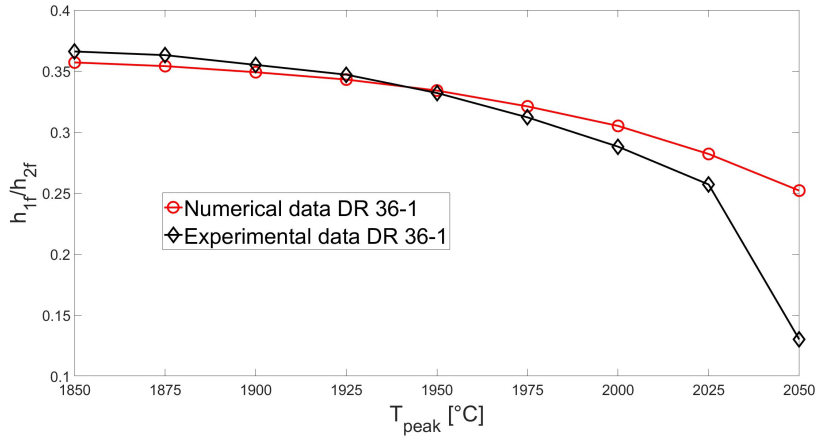


Figure 5. Comparison between the final external diameter of the capillary obtained numerically and experimentally by Luzi et al. [20] for the three different drawing ratios (**a**) DR36-1, (**b**) 54-15, and (**c**) 72-2 at different furnace peak temperatures.

(**a**)



(**b**)

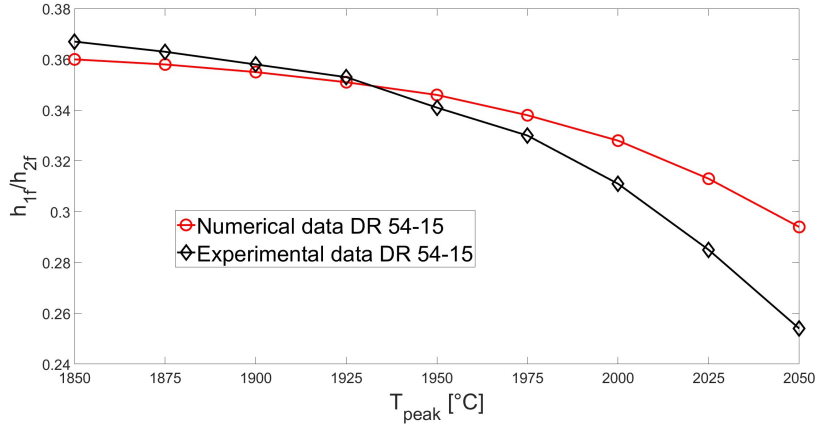


Figure 6. *Cont.*

(**c**)

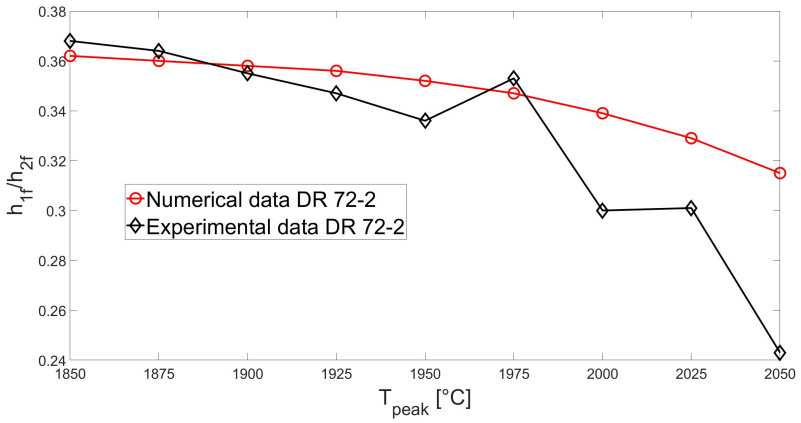
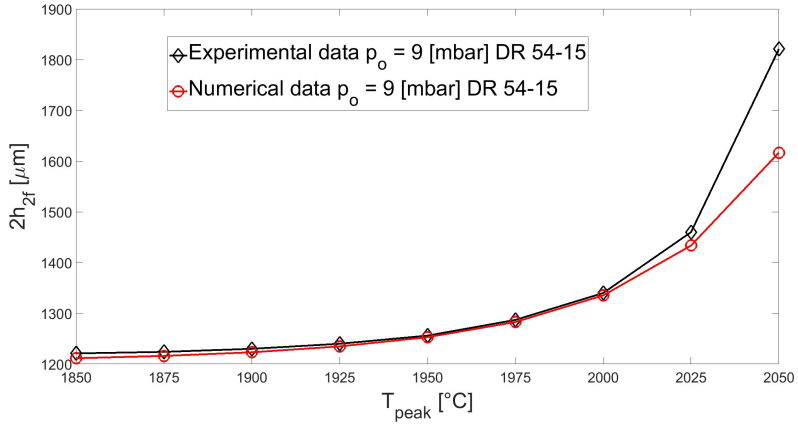


Figure 6. Comparison between the final air-filling fraction of the capillary obtained numerically and experimentally by Luzi et al. [20] for the three different drawing ratios (**a**) DR36-1, (**b**) 54-15, and (**c**) 72-2 at different furnace peak temperatures.

(**a**)



(**b**)

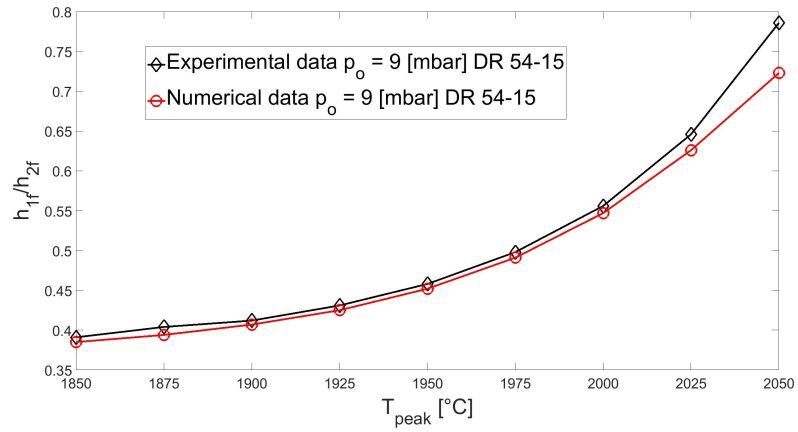


Figure 7. Comparison between the final outer diameter (**a**) and air-filling fraction (**b**) of the capillary obtained numerically and experimentally by Luzi et al. [20] for different furnace peak temperatures with a fixed value of internal pressurization.

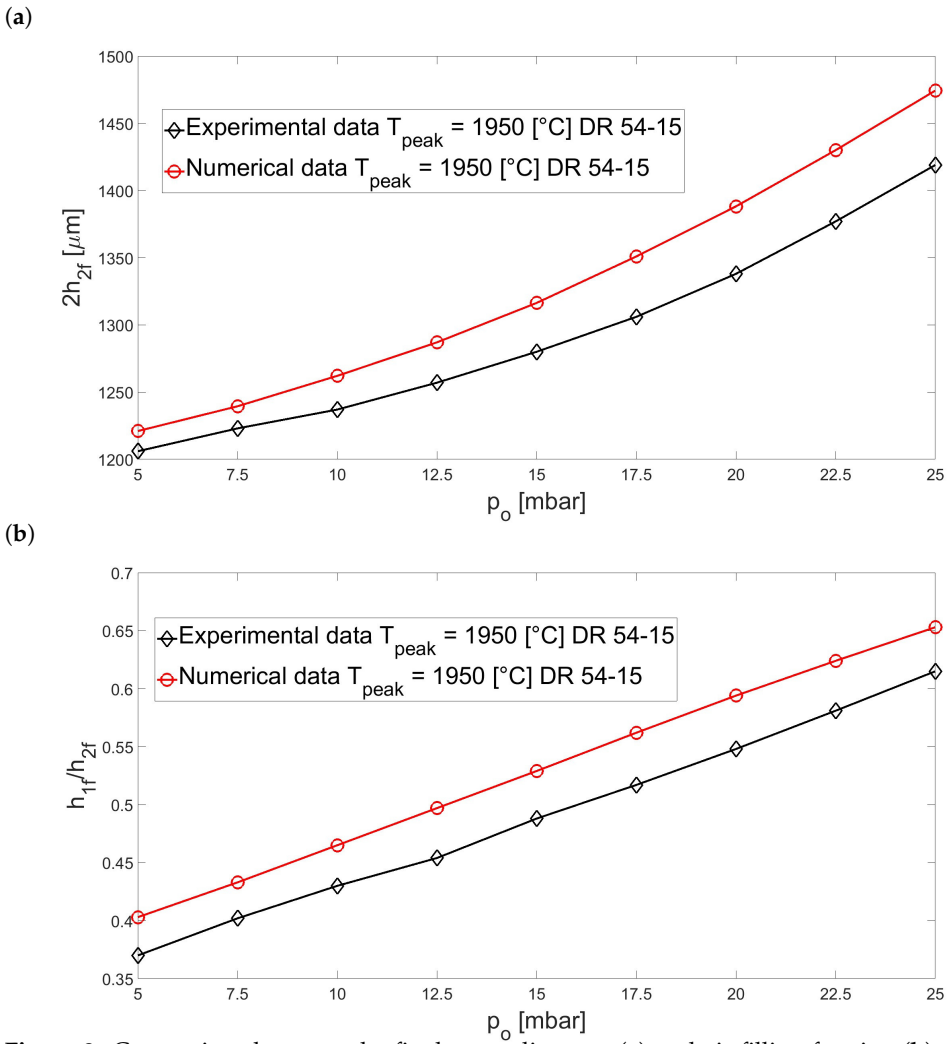


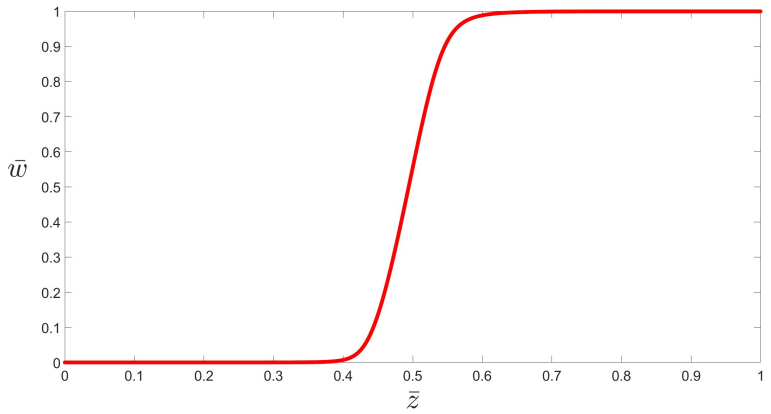
Figure 8. Comparison between the final outer diameter (**a**) and air-filling fraction (**b**) of the capillary obtained numerically and experimentally by Luzi et al. [20] for different values of internal pressurization and a fixed value of the furnace peak temperature.

4.3. High Drawing Ratios

In this section, we present exemplary results for the case of the high drawing ratio DR 1-102. This is relevant for fibre drawing, as the final dimensions of the capillary are of the same order of magnitude as commercially available optical fibres. Because the drawing speed is approximately ten times higher compared to the cases of the slow drawing ratios analyzed before, a smaller step size in the axial direction is required. Furthermore, because we realized that the temperature variations in the radial direction were not significant for the cases of the slow drawing ratios, we utilized a larger step size in the radial direction in the case of this high drawing ratio. This allowed us to choose a step size in the axial direction smaller than the one used with the slow drawing ratios, while it is not excessively small due to the constraint imposed by the Courant number for the stability of an explicit method. Moreover, we utilize Equation (33) to compute the Nusselt number β in the case of the high drawing ratio, as Equation (32) delivers values that are extremely high, promoting an unreasonable convective heat exchange that cools down the capillary too much and makes the numerical computations unstable. The high values of β are due to the high values of the axial velocity and the low values of the capillary size attained at the end of the drawing stage. Figure 9a shows that the axial velocity profile abruptly increases from a value approximately close to zero at $\overline{z} \approx 0.4$ up to about one at $\overline{z} \approx 0.6$. The increase of the axial velocity profile is steeper and the final value is attained at a shorter distance

compared to the slow drawing ratios. In addition, the inner and outer surfaces of the capillary shrink considerably during the drawing process, and the final size of the capillary is very thin; see Figure 9b and inset. With regard to the temperature distribution within the capillary, we notice the absence of a significant variation of the temperature with the radial direction; see the inset of Figure 9c. Furthermore, in this case the temperature distribution in the axial direction is very close to that of the furnace until $\bar{z} \approx 0.45$. Afterwards, the temperature profile of the capillary significantly departs from that of the furnace, assuming lower values until the exit of the furnace is reached; see Figure 9c. The dimensionless values of the temperature of the capillary at different radial positions at the exit of the oven are approximately equal to 0.7, while the dimensionless value of the furnace temperature at the exit of the furnace is approximately equal to 0.82. In Figure 10, we compare the values of the final external diameters and those of the air volume fractions obtained numerically and experimentally for different values of the peak temperature without internal pressurization. The deviations between experiments and numerical simulations reach a maximum of approximately 12 % (see Figure 10a) and is again achieved at a high peak temperatures, that is, T_{peak} = 2050 °C.

(**a**)



(**b**)

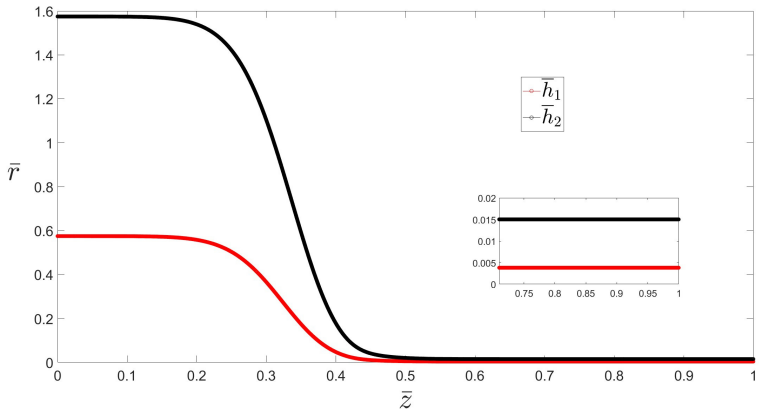


Figure 9. *Cont.*

(**c**)

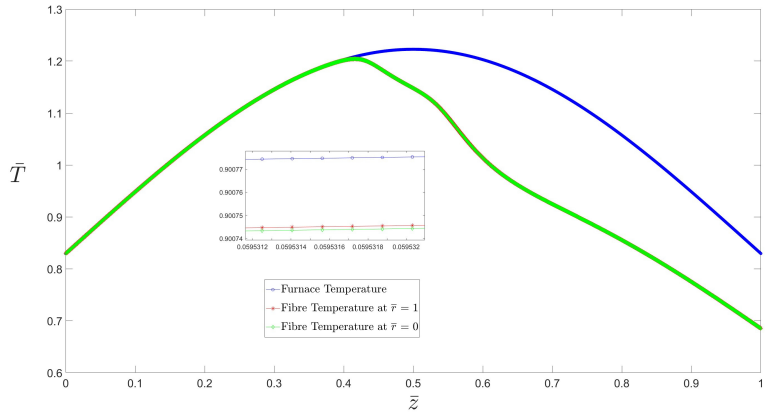
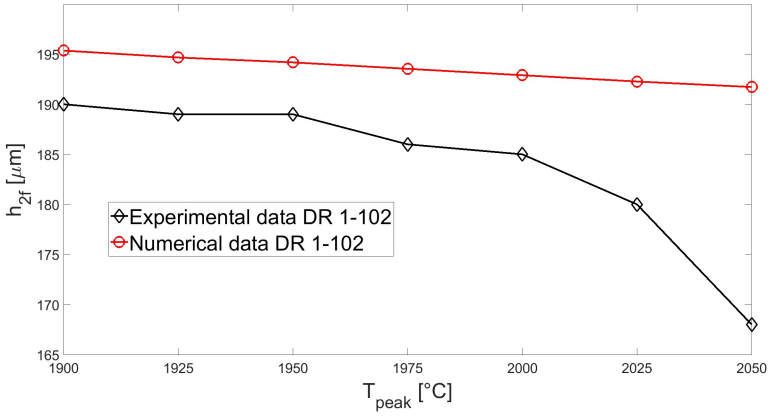


Figure 9. (**a**) Axial component of the velocity $\overline{w}$ against the axial distance $\overline{z}$, with $\overline{h}_1$ and $\overline{h}_2$ plotted against the axial distance $\overline{z}$ in (**b**) and the temperature profiles of the inner and outer capillary surfaces and the temperature profile of the furnace plotted against the axial distance $\overline{z}$ in (**c**). The inset in (**c**) shows the difference among the temperature profiles.

(**a**)



(**b**)

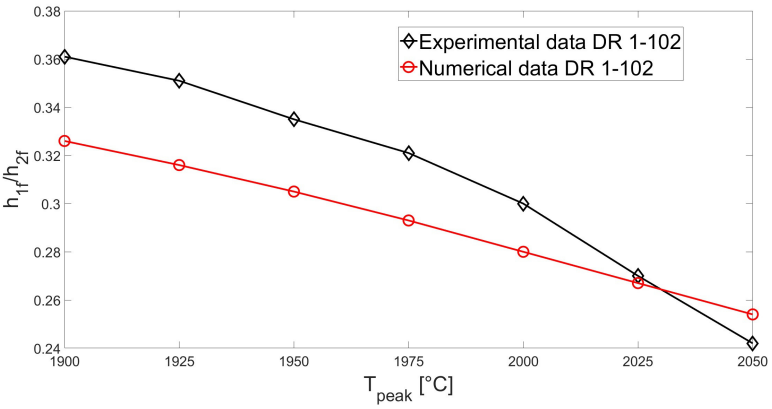


Figure 10. Comparison between the final outer diameter (**a**) and air-filling fraction (**b**) of the capillary obtained numerically and experimentally by Luzi et al. [20] for different furnace peak temperatures.

5. Discussion

In this work, we built a full asymptotic extensional-flow model to describe the evolution of a capillary during the drawing process. To this end, we analyzed and revisited the work of Taroni et al. [24] and integrated a new asymptotic energy equation into the

momentum and mass conservation equations of Fitt et al. [19]. To check the validity of the model, we compared the numerical outcomes with the experimental data of Luzi et al. [20] for the case of low and high drawing ratios with and without internal pressurization. In the derivation of the energy equation, we considered conductive, convective, and radiative heat exchange, assuming that the capillary is optically thick. In addition, we included the effects of viscous dissipation in our model, as it may significantly affect the reduction of the size of the capillary [49]. Yin and Yaluria [39] pointed out that viscous dissipation must not be neglected, as it becomes important in the stage of the drawing where the size of the capillary shrinks due to the viscosity assuming large values and the velocity gradients being significant. To consider a general situation, we allow the temperature to depend on the axial and radial position of the capillary, thus choosing an approach where the convection is balanced by the transport across the capillary and by viscous dissipation effects. In the case of slow drawing ratios, the asymptotic model forecasts a slight reduction of the fibre temperature profile once the capillary size starts to decrease. In the case of high-speed ratios, however, the model predicts a sharp decrease of the capillary temperature profile toward the end of the drawing process compared to the initial phase, where thermal equilibrium prevails and the temperature of the capillary closely matches that of the furnace. The trend of this temperature profile of the capillary resembles the asymmetric fibre temperature profile utilized by Luzi et al. [28] to model the drawing process of a six-hole optical fibre. This fibre temperature profile sharply decreases when the size of the preform contracts and the axial velocity increases. In the contribution of Luzi et al. [28], it is shown that the use of an asymmetric temperature profile produces numerical results that are in good accordance with the experimental outcomes. On the other hand, the choice of a symmetric Gaussian temperature profile with a large width may produce completely incorrect results, even leading to the explosion of a capillary [20]. The asymmetric capillary temperature profile is produced by the selected functional forms of the Nusselt number β, that is, Equations (32) and (33). They result from the choice of the functional forms of the convective heat exchange k_h, i.e., Equations (29) and (30). Yin and Jaluria [39] remark that the heat transfer due to the radiative heat exchange is small at the end of the drawing, as it is directly proportional to the surface area of the fibre. This is reduced by approximately 1000 times from the beginning to the end of the drawing process. Thereby, the convective heat transfer may become the prevailing heat transfer mechanism because of the increase of the velocity at the end of the drawing. To compute k_h, we utilized the correlation by Patel et al. [43] in the case of high drawing ratios, and the one suggested by Geyling and Homsy [42] in the case of slow drawing ratios. The correlation suggested by Geyling and Homsy [42] produces extremely high values of the maximum Nusselt number β_{max} in the case of the high drawing ratio. In fact, $\beta_{max} \approx 28.04$ if the correlation of Geyling and Homsy is utilized, while $\beta_{max} \approx 5.02$ when the correlation by Patel et al. [43] is applied. This implies that $k_{hmax} \approx 257 \left[\frac{W}{m^2K}\right]$ using the correlation of Geyling and Homsy, and $k_{hmax} \approx 46 \left[\frac{W}{m^2K}\right]$ employing the correlation by Patel et al. [43]. This result is close to the values obtained by Choudhury and Yaluria [50], who numerically computed the heat transfer coefficient while investigating the drawing process of solid glass fibres. The results of our simulations reveal that the temperature profile of the capillary does not vary significantly in the radial direction due to the small size of the preform. A similar result was obtained by Taroni et al. [24] within approximately 1 cm of a solid fibre preform employing the surface radiation parameter $\gamma_R = 5$. In our case, $\gamma_R = 5.3$ indicates that the bulk radiation is predominant and the temperature distribution is approximately constant across the capillary. The results of our numerical simulations match very well overall with the experiments by Luzi et al. [20], except for a few isolated cases where the discrepancies are very high. This happens for high values of the peak temperature, where the temperature profile may not be well approximated by the relation (26). As a result, the partial collapse of the inner radius of the capillary resulting from the competition between viscosity and surface tension may not be captured. The agreement between experiments

and simulations could be improved by utilizing a different correlation to model the furnace temperature profiles at high peak temperatures and an adequate correlation for the surface tension dependency on the temperature. Measurements of the furnace temperature profile are very difficult and prohibitive at high values of the furnace peak temperature [22], as thermocouples lose their accuracy and are inclined to melt. In addition, experimental and numerical investigations could be carried out to find different correlations for the convective heat transfer coefficient, as the models utilized to date have been developed for a solid thread [43] and for flow past a cylinder [42]. In addition, the present mathematical framework serves as a basis for modeling the drawing process of polymer optical fibres (POFs). As a first approximation, if the assumption of a Newtonian fluid is retained [25], the present mathematical formulation can be used in a straightforward way to model the drawing process of polymer axis-symmetric capillaries, as only a few process parameters need to be adjusted. However, because an adequate nonlinear viscoelastic model is necessary to accurately model the viscosity variations during the drawing of POFs, the governing equations need to be modified in a later stage of the research. Although the present asymptotic energy equation is only valid for annular capillaries and not for the general case of PCFs with arbitrary cross-sections, it provides a basis to improve simple models developed for more complicated geometries. For instance, the effects of viscous diffusion and the optically thick approximation can be included in the one-dimensional thermal model by Stokes et al. [34]. Moreover, this model can be extended to three dimensions, and work in this direction is currently ongoing.

6. Conclusions

In this work, we developed a novel asymptotic energy equation for the drawing process of an annular capillary. By coupling it with the mass, momentum, and evolution equations for the inner and outer surfaces by Fitt et al. [19], we built a complete asymptotic model for the capillary drawing process. The asymptotic system of equations is considerably simpler to solve numerically than the original full three-dimensional system of equations while being able to consider the main effects of heat transport across the capillary by convection, diffusion, and viscous dissipation. Heat is exchanged between the furnace and the capillary by convective and radiative mechanisms. To consider radiation within the capillary, we utilized the optically thick approximation and added an extra term to the conductive heat transfer coefficient. Although the validity of an optically thick capillary is likely to break down when the size of the capillary becomes very small, it nonetheless allows for quick and reliable computations of the geometry of the capillary compared to more involved approaches. Comparisons with experimental results for slow and high drawing ratios comprehensively show very good agreement for both pressurized and unpressurized capillaries. Discrepancies between experiments and simulations may be alleviated by a better choice of the value of the surface tension and a different correlation for the heat transfer coefficient.

Author Contributions: Supervision, B.G. and A.D.; Writing—original draft, S.L.; Writing—review & editing, G.L. All authors have read and agreed to the published version of the manuscript.

Funding: This work was supported by a National Research Foundation of Korea (NRF) grant funded by the Korean government (MSIT) (NRF-2021R1F1A1050103).

Institutional Review Board Statement: Not applicable.

Informed Consent Statement: Not applicable.

Data Availability Statement: Not applicable.

Conflicts of Interest: The authors declare no conflict of interest.

Appendix A

Appendix A.1. Two-Dimensional Mass and Momentum Equations for the Case of a Rotating Capillary

We assume axis-symmetry and an incompressible flow, i.e., $\rho = const$ and $\frac{\partial}{\partial \phi} = 0$, with a finite and non-zero v. The mass conservation equation assumes the same form as Equation (6), and many terms of the components of the stress tensor are identical to those defined in Section 2.1.2 for the case of a non-rotating capillary. The only components of the stress tensor that differ are

$$\tau_{r\phi} = \mu \left[r \frac{\partial}{\partial r} \left(\frac{v}{r} \right] \right)$$

and

$$\tau_{\phi z} = \mu \left(\frac{\partial v}{\partial z} \right)$$

The momentum equations along the radial and the azimuthal direction assume the form

$$\begin{aligned} \rho \left(\frac{\partial u}{\partial t} + u \frac{\partial u}{\partial r} - \frac{v^2}{r} + w \frac{\partial u}{\partial z} \right) &= f_r - \frac{\partial p}{\partial r} \\ + \frac{2}{r} \frac{\partial}{\partial r} \left(r \mu \left(\frac{\partial u}{\partial r} \right) \right) + \frac{\partial}{\partial z} \left(\mu \left(\frac{\partial w}{\partial r} + \frac{\partial u}{\partial z} \right) \right) &- 2 \mu \frac{u}{r^2} \end{aligned} \tag{A1}$$

$$\begin{aligned} \rho \left(\frac{\partial v}{\partial t} + u \frac{\partial v}{\partial r} + \frac{uv}{r} + w \frac{\partial v}{\partial z} \right) &= f_\phi + \frac{1}{r^2} \frac{\partial}{\partial r} \left[r^2 \mu \frac{\partial}{\partial r} \left(\frac{v}{r} \right) \right] \\ &+ \frac{\partial}{\partial z} \left(\mu \frac{\partial v}{\partial z} \right) \end{aligned} \tag{A2}$$

while the one along the axial direction is identical to Equation (8). The kinematic and dynamic boundary conditions defined in the previous section for the case of a non-rotating capillary hold for the present case as well. In addition, we have two more tangential boundary conditions

$$\boldsymbol{s}_1^T \cdot \boldsymbol{\tau} \cdot \boldsymbol{n}_1 = 0 \tag{A3a}$$

$$\boldsymbol{s}_2^T \cdot \boldsymbol{\tau} \cdot \boldsymbol{n}_2 = 0 \tag{A3b}$$

in the tangential azimuthal direction. Now, the stress tensor $\boldsymbol{\tau}$ reads

$$\boldsymbol{\tau} = \begin{bmatrix} 2\mu \left(\frac{\partial w}{\partial z} \right) - p & \mu \left(\frac{\partial v}{\partial z} \right) & \mu \left(\frac{\partial w}{\partial r} + \frac{\partial u}{\partial z} \right) \\ \mu \left(\frac{\partial v}{\partial z} \right) & 2\mu \left(\frac{\partial v}{\partial r} \right) - p & \mu \left[r \frac{\partial}{\partial r} \left(\frac{v}{r} \right) \right] \\ \mu \left(\frac{\partial w}{\partial r} + \frac{\partial u}{\partial z} \right) & \mu \left[r \frac{\partial}{\partial r} \left(\frac{v}{r} \right) \right] & 2\mu \left(\frac{\partial u}{\partial r} \right) - p \end{bmatrix} \tag{A4}$$

and

$$\boldsymbol{s}_1^T = \boldsymbol{s}_2^T = 1 \boldsymbol{e}_\phi$$

while $\boldsymbol{n}_i$ and $\boldsymbol{\tau}_i$ take the same form as Equations (11c) and (11b) for the case of a non-rotating capillary.

Appendix A.2. Energy Equation for the Case of a Rotating Capillary

In the case of a rotating capillary, the energy equation reads

$$\begin{aligned}\rho c_p\left(\frac{\partial T}{\partial t}+u\frac{\partial T}{\partial r}+w\frac{\partial T}{\partial z}\right)&=\frac{1}{r}\frac{\partial}{\partial r}\left(kr\frac{\partial T}{\partial r}\right)+\frac{\partial}{\partial z}\left(k\frac{\partial T}{\partial z}\right)\\&+2\mu\left[\left(\frac{\partial u}{\partial r}\right)^2+\left(\frac{u}{r}\right)^2+\left(\frac{\partial w}{\partial z}\right)^2\right]+\mu\left[r\frac{\partial}{\partial r}\left(\frac{v}{r}\right)\right]^2\\&+\mu\left(\frac{\partial v}{\partial z}\right)^2+\mu\left[\frac{\partial u}{\partial z}+\frac{\partial w}{\partial r}\right]^2\end{aligned}\tag{A5}$$

Employing the Rosseland approximation and using Equation (15), we obtain

$$\begin{aligned}\rho c_p\left(\frac{\partial T}{\partial t}+u\frac{\partial T}{\partial r}+w\frac{\partial T}{\partial z}\right)&=\frac{1}{r}\frac{\partial}{\partial r}\left(k_c r\frac{\partial T}{\partial r}\right)\\&+\frac{1}{r}\frac{\partial}{\partial r}\left(\tilde{k}_r r\frac{\partial T^4}{\partial r}\right)+\frac{\partial}{\partial z}\left(k_c\frac{\partial T}{\partial z}\right)+\frac{\partial}{\partial z}\left(\tilde{k}_r\frac{\partial T^4}{\partial z}\right)\\&+2\mu\left[\left(\frac{\partial u}{\partial r}\right)^2+\left(\frac{u}{r}\right)^2+\left(\frac{\partial w}{\partial z}\right)^2\right]+\mu\left[\frac{\partial u}{\partial z}+\frac{\partial w}{\partial r}\right]^2\\&\mu\left[r\frac{\partial}{\partial r}\left(\frac{v}{r}\right)\right]^2+\mu\left(\frac{\partial v}{\partial z}\right)^2\end{aligned}\tag{A6}$$

Appendix A.3. Non-Dimensionalization of the Governing Equations in the Case of a Rotating Capillary

We non-dimensionalize Equations (6), (8), (A1), (A2) and (A6) by setting

$$\begin{aligned}r&=\epsilon L\bar{r} & z&=L\bar{z} & u&=\epsilon W_1\bar{u}\\w&=W_1\bar{w} & h_1&=\epsilon L\bar{h}_1 & h_2&=\epsilon L\bar{h}_2\\p&=\frac{\mu_s W_1}{\epsilon^2 L}\bar{p} & T&=T_s\bar{T} & t&=\frac{L}{W_1}\bar{t}\\v&=\Omega L\bar{v} & \mu&=\mu_s\bar{\mu} & \phi&=\bar{\phi}\end{aligned}$$

where overbars indicate non-dimensional quantities, ϕ is the azimuthal angle, and Ω is the angular frequency. The continuity and momentum equations in the z direction are equal to Equation (19) and Equation (20), respectively. In turn, the equations in the r and in the ϕ direction assume the form

$$\begin{aligned}\epsilon^2 Re\left(\frac{\partial\bar{u}}{\partial\bar{t}}+\bar{u}\frac{\partial\bar{u}}{\partial\bar{r}}+\bar{w}\frac{\partial\bar{u}}{\partial\bar{z}}-\frac{S^2\bar{v}^2}{\epsilon^2\bar{r}}\right)&=\epsilon\frac{Re}{Fr^2}-\frac{\partial\bar{p}}{\partial\bar{r}}\\+\frac{2}{\bar{r}}\frac{\partial}{\partial\bar{r}}\left[\bar{r}\,\bar{\mu}\left(\frac{\partial\bar{u}}{\partial\bar{r}}\right)\right]+\epsilon^2\frac{\partial}{\partial\bar{z}}\left[\bar{\mu}\left(\frac{\partial\bar{u}}{\partial\bar{z}}\right)\right]+\frac{\partial}{\partial\bar{z}}\left[\bar{\mu}\left(\frac{\partial\bar{w}}{\partial\bar{r}}\right)\right]-2\bar{\mu}\left(\frac{\bar{u}}{\bar{r}^2}\right)\end{aligned}\tag{A7}$$

$$\begin{aligned}Re\left(\frac{\partial\bar{v}}{\partial\bar{t}}+\bar{u}\frac{\partial\bar{v}}{\partial\bar{r}}+\bar{w}\frac{\partial\bar{v}}{\partial\bar{z}}+\frac{\bar{u}\,\bar{v}}{\bar{r}}\right)&=\\\frac{1}{\epsilon^2\bar{r}^2}\frac{\partial}{\partial\bar{r}}\left[\bar{r}^2\,\bar{\mu}\left(\bar{r}\frac{\partial}{\partial\bar{r}}\left(\frac{\bar{v}}{\bar{r}}\right)\right)\right]+\frac{\partial}{\partial\bar{z}}\left[\bar{\mu}\left(\frac{\partial\bar{v}}{\partial\bar{z}}\right)\right]\end{aligned}\tag{A8}$$

The energy equation now reads

$$\begin{aligned}\epsilon^2 Pe\left(\frac{\partial \overline{T}}{\partial \overline{t}}+\overline{u}\frac{\partial \overline{T}}{\partial \overline{r}}+\overline{w}\frac{\partial \overline{T}}{\partial \overline{z}}\right)&=\frac{1}{\overline{r}}\frac{\partial}{\partial \overline{r}}\left(\overline{r}\frac{\partial \overline{T}}{\partial \overline{r}}\right)\\ +\frac{1}{\overline{r}}\frac{\partial}{\partial \overline{r}}\left(\gamma_R\overline{r}\frac{\partial \overline{T}^4}{\partial \overline{r}}\right)+\epsilon^2\frac{\partial}{\partial \overline{z}}\left(\frac{\partial \overline{T}}{\partial \overline{z}}\right)+\epsilon^2\frac{\partial}{\partial \overline{z}}\left(\gamma_R\frac{\partial \overline{T}^4}{\partial \overline{z}}\right)\\ +2\epsilon^2 Br\overline{\mu}\left[\left(\frac{\partial \overline{u}}{\partial \overline{r}}\right)^2+\left(\frac{\overline{u}}{\overline{r}}\right)^2+\left(\frac{\partial \overline{w}}{\partial \overline{z}}\right)^2\right]+\epsilon^2 Br\overline{\mu}\left[\frac{\partial \epsilon\overline{u}}{\partial z}+\frac{\partial \overline{w}}{\partial \epsilon\overline{r}}\right]^2\\ +\epsilon^2 Br_R\overline{\mu}\left(\frac{\partial \overline{v}}{\partial \overline{z}}\right)^2+\epsilon^2 Br_R\overline{\mu}\left[\overline{r}\frac{\partial}{\partial \overline{r}}\left(\frac{\overline{v}}{\epsilon\overline{r}}\right)\right]^2\end{aligned} \tag{A9}$$

where

$$Br_R=\frac{\mu_s\Omega^2L^2}{T_sk_c}$$

is the Brinkman number associated with the rotational speed and $S=\frac{\Omega L}{W_1}$. The dimensionless kinematic, normal, and axial tangential boundary conditions are the same as in Equations (23) and (24). The tangential boundary conditions in the azimuthal direction for the inner and outer surface read

$$\left.\frac{\partial \overline{v}}{\partial \overline{r}}\right|_{\overline{r}=\overline{h}_1}-\left.\frac{\overline{v}}{\overline{r}}\right|_{\overline{r}=\overline{h}_1}-\epsilon^2\frac{\partial \overline{h}_1}{\partial \overline{z}}\frac{\partial \overline{v}}{\partial \overline{z}}=0 \tag{A10a}$$

$$\left.\frac{\partial \overline{v}}{\partial \overline{r}}\right|_{\overline{r}=\overline{h}_2}-\left.\frac{\overline{v}}{\overline{r}}\right|_{\overline{r}=\overline{h}_2}-\epsilon^2\frac{\partial \overline{h}_2}{\partial \overline{z}}\frac{\partial \overline{v}}{\partial \overline{z}}=0 \tag{A10b}$$

Finally, the dimensionless thermal boundary conditions for the outer and the inner surface are equal to Equations (25).

Appendix A.4. Final Asymptotic Equations for the Case of a Rotating Capillary

In this case, we expand the unknowns as follows:

$$\begin{aligned}\overline{w}&=\overline{w}_0(\overline{t},\overline{z})+\epsilon^2\overline{w}_1(\overline{t},\overline{z},\overline{r})\\ \overline{u}&=\overline{u}_0(\overline{t},\overline{z},\overline{r})+\epsilon^2\overline{u}_1(\overline{t},\overline{z},\overline{r})\\ \overline{v}&=\overline{v}_0(\overline{t},\overline{z},\overline{r})+\epsilon^2\overline{v}_1(\overline{t},\overline{z},\overline{r})\\ \overline{p}&=\overline{p}_a+\epsilon^2\overline{P}(\overline{t},\overline{z},\overline{r})\\ \overline{T}&=\overline{T}_0(\overline{t},\overline{z},\overline{r})+\epsilon^2\overline{T}_1(\overline{t},\overline{z},\overline{r})\end{aligned}$$

including the azimuthal component of the velocity field $\overline{v}$, then use them in the non-dimensional continuity (Equation (19)), momentum (Equations (20), (A7) and (A8)), and energy (Equation (A9)) equations and boundary conditions (Equations (23), (24) and (A10)). We obtain the equations of Voyce et al. [21] by expanding the unknowns up to order ϵ^2, as follows:

$$\frac{\partial(\overline{h}_1^2\overline{w}_0)}{\partial \overline{z}}=\frac{2\overline{p}_0\overline{h}_2^2\overline{h}_1^2-2\overline{\gamma}\overline{h}_2\overline{h}_1(\overline{h}_2+\overline{h}_1)+ReS^2\overline{B}^2\,\overline{h}_1^2\overline{h}_2^2(\overline{h}_2^2-\overline{h}_1^2)}{2\overline{\mu}(\overline{h}_2^2-\overline{h}_1^2)} \tag{A11}$$

$$\frac{\partial(\overline{h}_2^2\overline{w}_0)}{\partial \overline{z}}=\frac{2\overline{p}_0\overline{h}_2^2\overline{h}_1^2-2\overline{\gamma}\overline{h}_2\overline{h}_1(\overline{h}_2+\overline{h}_1)+ReS^2\overline{B}^2\,\overline{h}_1^2\overline{h}_2^2(\overline{h}_2^2-\overline{h}_1^2)}{2\overline{\mu}(\overline{h}_2^2-\overline{h}_1^2)} \tag{A12}$$

$$\frac{\partial}{\partial \overline{z}}\left(3\overline{\mu}\frac{\partial \overline{w}_0}{\partial \overline{z}}(\overline{h}_2^2-\overline{h}_1^2)+\overline{\gamma}(\overline{h}_2+\overline{h}_1)+\frac{1}{4}ReS^2\overline{B}^2(\overline{h}_2^4-\overline{h}_1^4)\right)=0 \tag{A13}$$

$$\frac{\partial}{\partial\overline{z}}\left(\overline{\mu}\frac{\partial\overline{B}}{\partial\overline{z}}(\overline{h}_2^4-\overline{h}_1^4))\right)=Re\overline{w}_0\left[\overline{h}_2^2\frac{\partial}{\partial\overline{z}}\left(\overline{h}_2^2\overline{B}\right)-\overline{h}_1^2\frac{\partial}{\partial\overline{z}}\left(\overline{h}_1^2\overline{B}\right)\right]+\overline{h}_1^2\overline{h}_2^2\overline{B}\frac{Re\overline{p}_0}{\overline{\mu}}$$
$$+\frac{Re^2S^2\overline{h}_1^2\overline{h}_2^2\overline{B}^3\left(\overline{h}_2^2-\overline{h}_1^2\right)}{2\overline{\mu}}-\left(\overline{h}_1+\overline{h}_2\right)\frac{Re\overline{\gamma}\overline{B}\overline{h}_1\overline{h}_2}{\overline{\mu}} \tag{A14}$$

Equations (A11)–(A14) are the equations for the inner and outer fibre radii, axial momentum, and non-dimensional angular frequency equation, respectively; for more details, see [21]. Additionally, in this case we consider the steady-state situation and neglect the convective inertial terms in Equation (A13). As far as the energy equation is concerned, we rescale the Péclet and Brinkman numbers as follows:

$$Pe=\frac{\widetilde{P}}{\epsilon^2},\qquad Br=\frac{\widetilde{Br}}{\epsilon^2}\qquad Br_R=\frac{\widetilde{Br}_R}{\epsilon^2} \tag{A15}$$

obtaining

$$\widetilde{P}\left(\frac{\partial\overline{T}}{\partial\overline{t}}+\overline{u}\frac{\partial\overline{T}}{\partial\overline{r}}+\overline{w}\frac{\partial\overline{T}}{\partial\overline{z}}\right)=\frac{1}{\overline{r}}\frac{\partial}{\partial\overline{r}}\left(\overline{r}\frac{\partial\overline{T}}{\partial\overline{r}}\right)+\frac{1}{\overline{r}}\frac{\partial}{\partial\overline{r}}\left(\gamma_R\overline{r}\frac{\partial\overline{T}^4}{\partial\overline{r}}\right)$$
$$+2\widetilde{Br}\overline{\mu}\left[\left(\frac{\partial\overline{u}}{\partial\overline{r}}\right)^2+\left(\frac{\overline{u}}{\overline{r}}\right)^2+\left(\frac{\partial\overline{w}}{\partial\overline{z}}\right)^2\right]+\widetilde{Br}\overline{\mu}\left[\frac{\partial\epsilon\overline{u}}{\partial z}+\frac{\partial\overline{w}}{\partial\epsilon\overline{r}}\right]^2 \tag{A16}$$
$$+\widetilde{Br}_R\overline{\mu}\left(\frac{\partial\overline{v}}{\partial\overline{z}}\right)^2+\widetilde{Br}_R\overline{\mu}\left[\overline{r}\frac{\partial}{\partial\overline{r}}\left(\frac{\overline{v}}{\epsilon\overline{r}}\right)\right]^2$$

Using the coordinate system defined in Equation (40), the axial momentum equation becomes

$$\frac{\partial\overline{w}_0}{\partial\overline{\zeta}}=\left(\frac{\overline{F}-\overline{\gamma}(\overline{h}_2+\overline{h}_1)-\frac{1}{4}ReS^2\overline{B}^2(\overline{h}_2^4-\overline{h}_1^4)}{3\overline{\mu}(\overline{h}_{20}^2-\overline{h}_{10}^2)\overline{W}_0}\right)\overline{w}_0 \tag{A17}$$

where again the constant $\overline{F}$ is the tension required to pull the fibre. Utilizing the asymptotic expansions defined in this section and changing the variables in Equation (A16) according to Equation (40), we obtain

$$\frac{\partial\overline{T}}{\partial\overline{\zeta}}=\overline{\Psi}\frac{\partial\overline{T}_0}{\partial\overline{x}}+\overline{\Omega}\left(\frac{\partial^2\overline{T}_0}{\partial\overline{x}^2}\right)+\overline{\Lambda}\left(\frac{\partial\overline{T}_0}{\partial\overline{x}}\right)^2$$
$$+\frac{\widetilde{Br}\overline{\mu}}{\overline{w}_0}\left[3\left(\frac{\partial\overline{w}_0}{\partial\overline{\zeta}}\right)^2+\left(\frac{2\overline{A}_R}{\overline{\Theta}^2}\right)^2\right]+\frac{\widetilde{Br}_R\overline{\mu}}{\overline{w}_0}\left(\frac{\partial\overline{B}}{\partial\overline{\zeta}}\overline{\Theta}\right)^2 \tag{A18}$$

where

$$\overline{\Pi}=[\overline{x}(\overline{h}_2-\overline{h}_1)+\overline{h}_1](\overline{h}_2-\overline{h}_1)$$
$$\overline{\Theta}=[\overline{x}(\overline{h}_2-\overline{h}_1)+\overline{h}_1]$$
$$\overline{\Lambda}=\frac{12\gamma_R\overline{T}_0^2}{\overline{w}_0(\overline{h}_2-\overline{h}_1)^2}$$
$$\overline{\Omega}=\frac{1+4\gamma_R\overline{T}_0^3}{\overline{w}_0(\overline{h}_2-\overline{h}_1)^2}$$
$$\overline{\Psi}=\frac{1}{\overline{w}_0}\left[\frac{1+4\gamma_R\overline{T}_0^3}{\overline{\Pi}}-\frac{\overline{A}_R}{\overline{\Pi}}+\widetilde{P}\frac{\partial\overline{w}_0}{\partial\overline{\zeta}}\frac{\overline{\Theta}}{2(\overline{h}_2-\overline{h}_1)}\right]$$
$$\overline{A}_R=\frac{2\overline{p}_0\overline{h}_2^2\overline{h}_1^2-2\overline{\gamma}\overline{h}_2\overline{h}_1(\overline{h}_2+\overline{h}_1)-ReS^2\overline{B}^2(\overline{h}_2^2\overline{h}_1^4-\overline{h}_1^2\overline{h}_2^4)}{4\overline{\mu}(\overline{h}_2^2-\overline{h}_1^2)}$$

Finally, the thermal boundary conditions assume the same form as in Equation (46).

References

1. Russell, P.S. Photonic-Crystal Fibers. *J. Light. Technol.* **2006**, *24*, 4729–4749. [CrossRef]
2. Buczynski, R. Photonic Crystal Fibers. *Acta Phys. Pol. A* **2004**, *106*, 141–167. [CrossRef]
3. Humbert, G.; Knight, J.; Bouwmans, G.; Russell, P.; Williams, D.; Roberts, P.; Mangan, B. Hollow core photonic crystal fibers for beam delivery. *Opt. Express* **2004**, *12*, 1477–1484. [CrossRef] [PubMed]
4. Wadsworth, W.J.; Percival, R.M.; Bouwmans, G.; Knight, J.C.; Birks, T.A.; Hedley, T.D.; Russell, P.S.T. Very High Numerical Aperture Fibers. *IEEE Photonics Technol. Lett.* **2004**, *16*, 843–845. [CrossRef]
5. Di Teodoro, F.; Brooks, C.D. 1.1 MW peak-power, 7 W average-power, high-spectral-brightness, diffraction-limited pulses from a photonic crystal fiber amplifier. *Opt. Lett.* **2005**, *30*, 2694–2696. [CrossRef]
6. Chernikov, S.V.; Zhu, Y.; Taylor, J.R.; Gapontsev, V.P. Supercontinuum self-Q-switched ytterbium fiber laser. *Opt. Lett.* **1997**, *22*, 298–300. [CrossRef]
7. Dainese, P.; Russell, P.J.S.; Joly, N.; Knight, J.C.; Wiederhecker, G.S.; Fragnito, H.L.; Laude, V.; Khelif, A. Stimulated Brillouin scattering from multi-GHz-guided acoustic phonons in nanostructured photonic crystal fibres. *Nat. Phys.* **2006**, *2*, 388–392. [CrossRef]
8. Monro, T.M.; Belardi, W.; Furusawa, K.; Baggett, J.C.; Broderick, N.G.R.; Richardson, D.J. Sensing with microstructured optical fibres. *Meas. Sci. Technol.* **2001**, *12*, 854–858. [CrossRef]
9. Marques, C.A.F.; Pospori, A.; Demirci, G.; Çetinkaya, O.; Gawdzik, B.; Antunes, P.; Bang, O.; Mergo, P.; André, P.; Webb, D.J. Fast Bragg Grating Inscription in PMMA Polymer Optical Fibres: Impact of Thermal Pre-Treatment of Preforms. *Sensors* **2017**, *17*, 891. [CrossRef]
10. Emiliyanov, G.; Jensen, J.B.; Bang, O.; Hoiby, P.E.; Pedersen, L.H.; Kjaer, E.M.; Lindvold, L. Localized biosensing with Topas microstructured polymer optical fiber. *Opt. Lett.* **2007**, *32*, 460–462. [CrossRef]
11. Hu, X.; Chen, Y.; Gao, S.; Min, R.; Woyessa, G.; Bang, O.; Qu, H.; Wang, H.; Caucheteur, C. Direct Bragg Grating Inscription in Single Mode Step-Index TOPAS/ZEONEX Polymer Optical Fiber Using 520 nm Femtosecond Pulses. *Polymers* **2022**, *14*, 1350. [CrossRef] [PubMed]
12. Hu, X.; Woyessa, G.; Kinet, D.; Janting, J.; Nielsen, K.; Bang, O.; Caucheteur, C. BDK-doped core microstructured PMMA optical fiber for effective Bragg grating photo-inscription. *Opt. Lett.* **2017**, *42*, 2209–2212. [CrossRef]
13. van Eijkelenborg, M.A.; Argyros, A.; Barton, G.; Bassett, I.M.; Fellew, M.; Henry, G.; Issa, N.A.; Large, M.C.; Manos, S.; Padden, W.; et al. Recent progress in microstructured polymer optical fibre fabrication and characterisation. *Opt. Fiber Technol.* **2003**, *9*, 199–209. [CrossRef]
14. van Eijkelenborg, M.; Large, M.; Argyros, A.; Zagari, J.; Manos, S.; Issa, N.; Bassett, I.; Fleming, S.; McPhedran, R.; de Sterke, C.M.; et al. Microstructured polymer optical fibre. *Opt. Express* **2001**, *9*, 319–327. [CrossRef] [PubMed]
15. Argyros, A. Applications of microstructured polymer optical fibers. In Proceedings of the 2010 Photonics Global Conference, Singapore, 14–16 December 2010; pp. 1–4. [CrossRef]
16. Paek, U.C.; Runk, R.B. Physical behavior of the neck–down region during furnace drawing of silica fibers. *J. Appl. Phys.* **1978**, *49*, 4417–4422. [CrossRef]
17. Myers, M.R. A model for unsteady analysis of preform drawing. *AIChE J.* **1989**, *35*, 592–602. [CrossRef]
18. Glicksman, L.R. The Dynamics of a Heated Free Jet of Variable Viscosity Liquid at Low Reynolds Numbers. *J. Basic Eng.* **1968**, *90*, 343–354. [CrossRef]
19. Fitt, A.D.; Furusawa, K.; Monro, T.M.; Please, C.P.; Richardson, D.J. The mathematical modelling of capillary drawing for holey fibre manufacture. *J. Eng. Math.* **2002**, *43*, 201–227. [CrossRef]
20. Luzi, G.; Epple, P.; Scharrer, M.; Fujimoto, K.; Rauh, C.; Delgado, A. Influence of Surface Tension and Inner Pressure on the Process of Fibre Drawing. *J. Light. Technol.* **2010**, *28*, 1882–1888. [CrossRef]
21. Voyce, C.J.; Fitt, A.D.; Monro, T.M. The mathematical modelling of rotating capillary tubes for holey-fibre manufacture. *J. Eng. Math.* **2008**, *60*, 69–87. [CrossRef]
22. Voyce, C.J.; Fitt, A.D.; Monro, T.M. Mathematical Modeling as an Accurate Predictive Tool in Capillary and Microstructured Fiber Manufacture: The Effects of Preform Rotation. *J. Light. Technol.* **2008**, *26*, 791–798. [CrossRef]
23. Voyce, C.J.; Fitt, A.D.; Hayes, J.R.; Monro, T.M. Mathematical Modeling of the Self-Pressurizing Mechanism for Microstructured Fiber Drawing. *J. Light. Technol.* **2009**, *27*, 871–878. [CrossRef]
24. Taroni, M.; Breward, C.J.W.; Cummings, L.J.; Griffiths, I.M. Asymptotic solutions of glass temperature profiles during steady optical fibre drawing. *J. Eng. Math.* **2013**, *80*, 1–20. [CrossRef]
25. Xue, S.C.; Tanner, R.I.; Barton, G.W.; Lwin, R.; Large, M.; Poladian, L. Fabrication of microstructured optical fibers-part I: Problem formulation and numerical modeling of transient draw process. *J. Light. Technol.* **2005**, *23*, 2245–2254. [CrossRef]
26. Xue, S.C.; Tanner, R.I.; Barton, G.W.; Lwin, R.; Large, M.; Poladian, L. Fabrication of microstructured optical fibers-part II: Numerical modeling of steady-state draw process. *J. Light. Technol.* **2005**, *23*, 2255–2266. [CrossRef]
27. Xue, S.C.; Large, M.; Barton, G.W.; Tanner, R.I.; Poladian, L.; Lwin, R. Role of material properties and drawing conditions in the fabrication of microstructured optical fibers. *J. Light. Technol.* **2006**, *24*, 853–860. [CrossRef]

28. Luzi, G.; Epple, P.; Scharrer, M.; Fujimoto, K.; Rauh, C.; Delgado, A. Numerical Solution and Experimental Validation of the Drawing Process of Six-Hole Optical Fibers Including the Effects of Inner Pressure and Surface Tension. *J. Light. Technol.* **2012**, *30*, 1306–1311. [CrossRef]
29. Stokes, Y.M.; Buchak, P.; Crowdy, D.G.; Ebendorff-Heidepriem, H. Drawing of micro-structured fibres: circular and non-circular tubes. *J. Fluid Mech.* **2014**, *755*, 176–203. [CrossRef]
30. Chen, M.J.; Stokes, Y.M.; Buchak, P.; Crowdy, D.G.; Ebendorff-Heidepriem, H. Microstructured optical fibre drawing with active channel pressurisation. *J. Fluid Mech.* **2015**, *783*, 137–165. [CrossRef]
31. Buchak, P.; Crowdy, D.G.; Stokes, Y.M.; Ebendorff-Heidepriem, H. Elliptical pore regularisation of the inverse problem for microstructured optical fibre fabrication. *J. Fluid Mech.* **2015**, *778*, 5–38. [CrossRef]
32. Buchak, P.; Crowdy, D.G. Surface-tension-driven Stokes flow: A numerical method based on conformal geometry. *J. Comput. Phys.* **2016**, *317*, 347–361. [CrossRef]
33. Chen, M.J.; Stokes, Y.M.; Buchak, P.; Crowdy, D.G.; Ebendorff-Heidepriem, H. Asymptotic Modelling of a Six-Hole MOF. *J. Light. Technol.* **2016**, *34*, 5651–5656. [CrossRef]
34. Stokes, Y.M.; Wylie, J.J.; Chen, M.J. Coupled fluid and energy flow in fabrication of microstructured optical fibres. *J. Fluid Mech.* **2019**, *874*, 548–572. [CrossRef]
35. Jasion, G.T.; Shrimpton, J.S.; Chen, Y.; Bradley, T.; Richardson, D.J.; Poletti, F. MicroStructure Element Method (MSEM): Viscous flow model for the virtual draw of microstructured optical fibers. *Opt. Express* **2015**, *23*, 312–329. [CrossRef]
36. Lee, S.; Jaluria, Y. Simulation of the transport processes in the neck-down region of a furnace drawn optical fiber. *Int. J. Heat Mass Transf.* **1997**, *40*, 843–856. [CrossRef]
37. Roy Choudhury, S.; Jaluria, Y. Thermal transport due to material and gas flow in a furnace for drawing an optical fiber. *J. Mater. Res.* **1998**, *13*, 494–503. [CrossRef]
38. Yin, Z.; Jaluria, Y. Zonal Method to Model Radiative Transport in an Optical Fiber Drawing Furnace. *J. Heat Transf.* **1997**, *119*, 597–603. [CrossRef]
39. Yin, Z.; Jaluria, Y. Neck Down and Thermally Induced Defects in High-Speed Optical Fiber Drawing. *J. Heat Transf.* **2000**, *122*, 351–362. [CrossRef]
40. Xue, S.C.; Poladian, L.; Barton, G.W.; Large, M. Radiative heat transfer in preforms for microstructured optical fibres. *Int. J. Heat Mass Transf.* **2007**, *50*, 1569–1576. [CrossRef]
41. Schlichting, H.; Gersten, K. *Boundary-Layer Theory*, 9th ed.; Springer: Berlin/Heidelberg, Germany, 2017.
42. Geyling, F.; Homsy, G.M. Extensional instabilities of the glass fibre drawing process. *Glass Technol.* **1980**, *21*, 95–102.
43. Patel, R.M.; Bheda, J.H.; Spruiell, J.E. Dynamics and structure development during high-speed melt spinning of nylon 6. II. Mathematical modeling. *J. Appl. Polym. Sci.* **1991**, *42*, 1671–1682. [CrossRef]
44. Urbain, G.; Bottinga, Y.; Richet, P. Viscosity of liquid silica, silicates and alumino-silicates. *Geochim. Cosmochim. Acta* **1982**, *46*, 1061–1072. [CrossRef]
45. Hetherington, G.; Jack, K.H.; Kennedy, J.C. The viscosity of vitreous silica. *Phys. Chem. Glas.* **1964**, *5*, 130–136.
46. Doremus, R.H. Viscosity of silica. *J. Appl. Phys.* **2002**, *92*, 7619–7629. [CrossRef]
47. Huang, H.; Miura, R.M.; Wylie, J.J. Optical Fiber Drawing and Dopant Transport. *SIAM J. Appl. Math.* **2008**, *69*, 330–347. [CrossRef]
48. Lewis, J.A. The collapse of a viscous tube. *J. Fluid Mech.* **1977**, *81*, 129. [CrossRef]
49. Wylie, J.J.; HUANG, H. Extensional flows with viscous heating. *J. Fluid Mech.* **2007**, *571*, 359–370. [CrossRef]
50. Roy Choudhury, S.; Jaluria, Y. Practical aspects in the drawing of an optical fiber. *J. Mater. Res.* **1998**, *13*, 483–493. [CrossRef]